ABSTRACT

Title of dissertation: CONSTRUCTION OF APPARATUS AND FIRST EXPERIMENTS INVESTIGATING DYNAMICS OF BOSE-EINSTEIN CONDENSATES IN DISORDERED OPTICAL LATTICES

Emily Elisa Edwards, Doctor of Philosophy, 2009

Dissertation directed by: Professor Steven L. Rolston
Department of Physics

Since the experimental achievement of Bose-Einstein condensation (BEC) in dilute gases, ultra-cold atom systems have proven to be an unparalleled test bed for condensed matter phenomena. With this in mind, our laboratory set out to build an apparatus for the study of the effects of disorder on condensed matter phase transitions using a BEC loaded into one, two, and three-dimensional lattices. My thesis is divided into two main sections. In the first section I describe in detail the design and construction of our apparatus. Our system is designed to form ^{87}Rb condensates of approximately 10^5 atoms. We have three possible experimental science chambers.

1. One can perform 1D lattice experiments in the chamber where the condensate is formed. There is a mirror located in vacuum, which is suitable for this purpose.

2. In a glass chamber one can do 1D, 2D, or 3D lattice experiments. Atoms are loaded into a dipole trap (optical tweezer) prior to condensation and transported

approximately 20 cm to the glass cell where optical evaporation is performed to form a BEC.

3. One can transfer, using the same techniques as (2), to a chamber with a multi-channel plate detector for Rydberg atom experiments.

The experimental results described in my thesis pertain to situation (1). However, I describe some details of (2) in the construction section. The first experiment presented in my thesis demonstrates the effect of disorder on the time-dependent dynamics of lattice systems. We observe that a small perturbation produces a dramatic change in the adiabaticity criteria for loading a BEC into one-dimensional optical lattice. I conclude with experiments that we expect to perform on this apparatus.

CONSTRUCTION OF APPARATUS AND FIRST EXPERIMENTS INVESTIGATING DYNAMICS OF BOSE-EINSTEIN CONDENSATES IN DISORDERED OPTICAL LATTICES

by

Emily Elisa Edwards

Dissertation submitted to the Faculty of the Graduate School of the
University of Maryland, College Park in partial fulfillment
of the requirements for the degree of
Doctor of Philosophy
2009

Advisory Committee:
Professor Steven L. Rolston, Chair/Advisor
Professor Kristian Helmerson
Professor Victor Galitski
Professor Christopher Monroe
Professor Amy Mullin

Dedication

To my labmates.

Acknowledgments

I would like to thank my advisor, Prof. Steve Rolston for the opportunity to build an experiment and for mentoring me as a graduate student. Also, I would like to acknowledge and thank my lab mate Matthew Beeler, who has been my partner in this adventure and who is equally responsible for the apparatus. Additionally, I would like to acknowledge to the following previous and current colleagues who have contributed to this intellectual endeavor: Brendan Wyker, Dr. Kevin Teo, Jennifer Robinson, Ilya Arakelyan, Dr. Ian Spielman, Dr. Trey Porto, and Dr. Zhao-Yuan Ma. Additionally, I thank the group members, past and present, of the Rolston, Orozco, Monroe, and NIST laser cooling research groups for consultation and for lending equipment to us. Also, I would like to thank my friends and family for their support.

This work was funded by NASA, ARO, and NSF.

Table of Contents

List of Figures

List of Abbreviations

Rb	Rubidium
BEC	Bose-Einstein Condensate or Bose-Einstein Condensation
UHV	Ultra-high vacuum
MOT	Magneto-optical trap
psd	phase space density
IGBT	insulated gate bipolar transistor
NASA	National Aeronautics and Space Administration
ARO	Army Research Office
NSF	National Science Foundation
NIST	National Institutes of Standards and Technology
JQI	Joint Quantum Institute

Chapter 1

Introduction

1.1 Bose-Einstein Condensates

A comprehensive review of the history and theory of Bose-Einstein condensation (BEC) is given in [48, 12]. BEC was predicted in 1925 by Albert Einstein using the statistics of photons developed by Satyendra Bose and extending it to atoms. In the decades to follow, London suggested the existence of BEC in superfluid helium (He) which has been observed in neutron scattering experiments (see Refs. in [48, 12]). Additionally, superconductors are also a system exhibiting BEC behavior [33]. However, BEC could not be well-studied in these systems. BEC was first achieved experimentally at near zero temperature in dilute gases of alkali atoms in 1995 [1, 14]. Because of the robust nature of cold-atom experiments, BEC has proven to be an invaluable source of research connecting the atomic physics realm to condensed matter, fluid dynamics, quantum information, and even cosmological theories. Here, I briefly describe the essential background theory necessary to the understanding of our experiment.

The phase transition to BEC from a thermal state is a result of the statistics of bosons (integer spin particles). The most succinct description is "a macroscopic occupation of the ground state." For a system of non-interacting bosons, the occu-

pation number of a state with energy ϵ_ν is

$$n(\epsilon_\nu) = \frac{1}{e^{(\epsilon_\nu - \mu)/k_b T} - 1} \tag{1.1}$$

In Eq. 1.1 , T is temperature, k_b is Boltzmann's constant, and μ is the chemical potential. Unlike fermions, bosons can occupy the same state and it was predicted that for sufficiently low temperatures and high densities, a thermal ensemble will begin to have a large number of atoms occupying the lowest energy level of the system. One can calculate a critical temperature for this transition, $T = T_c$, by calculating the number of atoms in excited states of a uniform gas confined to a cube of volume, V, using

$$N_{ex} = \int_0^\infty d\epsilon g(\epsilon) n(\epsilon_\nu) \tag{1.2}$$

where $g(\epsilon)$ is the density of states. For the cube, the density of states is

$$g(\epsilon) = \frac{V M^{3/2}}{2^{1/2}\pi^2\hbar^3}\epsilon^{1/2} \tag{1.3}$$

where M is mass and $\hbar$ is Planck's constant [48]. By substituting Eq. 1.1 and Eq. 1.3 into Eq. 1.2 and solving for T_c when $\mu = 0$, one obtains

$$T_c \approx \frac{3.31\hbar^2 n^{2/3}}{M} \tag{1.4}$$

Here, n is the density of particles per unit volume , N/V. The phase space density (psd) is the number of particles in a volume whose length scale is the thermal deBroglie wavelength, $\lambda_{dB} = (2\pi\hbar^2/Mk_bT)^{1/2}$, and is the experimental parameter we optimize. One derives that the phase space density (psd) condition for BEC (uniform gas) is $n\lambda_{dB}^3 \geq 2.612$.

The critical parameters are slightly modified if we use a harmonic confining potential, having trapping frequencies $\omega_x, \omega_y, \omega_z$, which is our experimental situation. The density of states in this case is

$$g(\epsilon) = \frac{1}{2\hbar^3 \omega_x \omega_y \omega_z} \epsilon^2 \tag{1.5}$$

Solving for T_c one finds that the critical temperature depends on the harmonic trapping frequencies and the number of atoms, N.

$$T_c \approx \frac{0.94\hbar}{k_b} (\omega_x \omega_y \omega_z)^{1/3} N^{1/3} \tag{1.6}$$

Typical transition temperatures are sub-μK (in our system down to around 100 nK) for dilute gas systems. Densities for these cold atom systems are around $10^{13} - 10^{15}$ cm^{-3}. For more details see Refs. [48, 12].

Although dilute gas BECs were first thought to be an achievement in atomic physics with little relevance to other fields, they have emerged as tools for the study of a wide variety of interesting physical problems. For example, there is phase coherence across the condensate, which allows for diagnostic techniques and experiments in matter-wave interference, and continued research in developing an atom laser, a coherent source of matter waves. Additionally, a BEC in a dilute gas can be repeatably created using current technologies in under a minute which makes studying them very robust.

It was realized very quickly that BECs as sources of coherent atoms, coupled with periodic optical potentials (lattices), allows for the study of many condensed matter problems. The first clear demonstration of a condensed matter, many-body problem studied with BEC was the observation of the superfluid to Mott insulator

transition [26]. Much of the current BEC research is aimed at the study of various condensed matter phenomena, which are otherwise difficult to approach with solid state experiments[45, 8]. However, they are also used for studying quantum computing with neutral atoms [39] and look promising for the study of many-body dynamics in non-equilibrium systems [64, 20, 23] .

1.2 Overview of Thesis

The work described in this thesis is divided into two main parts. The first section is an overview of the construction of the BEC apparatus. I include the most details on the parts that I was personally involved in building, characterizing, and optimizing. In Chapter 3, I present an experiment studying the time-dependent dynamics of loading a BEC into a pseudo-disordered potential. Chapter 4 gives an overview of experiments that I have been involved in, but are in the early stages of development. The Appendices are helpful references for the user of the apparatus.

Chapter 2

Construction

In the beginning...There was an empty lab. The following is a description of what happened next.

As described in Chapter 1, theoretically there are only a few requirements for achieving a BEC in a harmonic trap: a bosonic sample with phase space density approximately equal to 1. In practice, there are many technological considerations that accompany this experiment. Here, I describe the main details of the design of our experiment. In each section, I explain the relevance to condensate formation. All of this work is performed under ultra-high vacuum (UHV) conditions, so creating this environment is the experimentalist's first task when embarking on BEC research. Then I will describe the theory and implementation of each stage of BEC formation. Appendix A gives a table with vendors and part numbers.

2.1 Vacuum System: UHV side

In order to create a suitable environment for the production of a BEC we needed to design a system with pressures on the order of 10^{-11} torr. This stringent requirement is a consequence of the time it takes to achieve BEC. In a magnetic trap, forced radio-frequency (rf) evaporation typically takes 20-30 seconds, which translates into needing a vacuum-limited lifetime at least comparable and preferably

longer than this time. Background collisions severely limit the lifetime of trapped atoms, thus the lower the pressure the better. A quick calculation, assuming no other loss mechanisms, shows that the vacuum limited lifetime of a magnetic trap is of order 200 s at 5×10^{-11} torr (lifetime$\sim 10^{-8}/P_{torr}$) [42]. The following is a description of our vacuum system in its current form.

The system, although originally a single chamber, was modified to include two chambers: the source side and the ultra-high vacuum (UHV)/science side. A schematic depicting the setup of the UHV/science-side with photos is shown in Fig. 2.1.

UHV is maintained in the science side of the chamber by a combination of a 150 L/s Varian Starcell (diode) double-ended ion pump and a titanium sublimation pump (Ti-sub), which is situated inside of the ion pump. We have two types of pumps because the ion pump is efficient at lowering the pressure due to most gases through ionization, whereas the Ti-sub pump releases titanium which is effective at pumping molecules like H_2 and H_2O. The Starcell type pump is an option which increases the efficiency of the pump for removing noble gases. The pressure is monitored by a dual filament nude Bayard-type ion gauge (Granville-Phillips). It should be noted that the ion pump is a poor pump for rubidium and will eventually fail after years of use. Also, the ion gauge will pump rubidium but also act as a diffusive source via outgassing, so it is not a very reliable measure of exact pressure. The best test of vacuum quality is the lifetime of the atoms in the magnetic trap measured after some evaporation.

The main chamber (where the condensate is formed) is a stainless steel Kim-

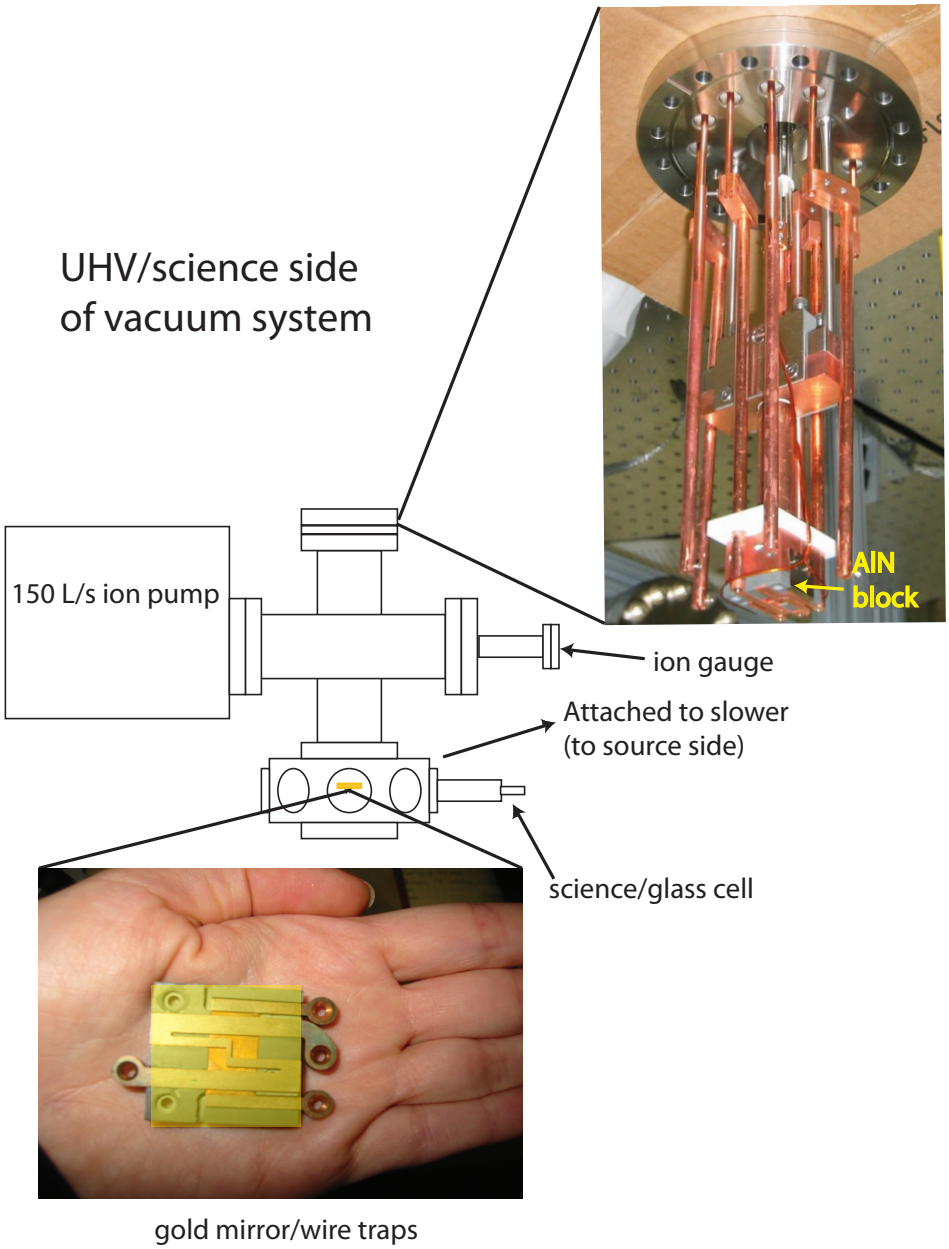

Figure 2.1: Layout of UHV side of the vacuum system with photos of the custom design feedthrough. The wire traps are shown with a false translucent gold mirror overlaid to clarify the physical location of the actual gold mirror.

ball Physics spherical octagon. The windows are anti-reflection coated (Spectrum Thin Films) for either 780 nm or 1550 nm light depending on their intended purpose. Most of the vacuum parts in both the source side and the science side are standard issue, with the notable exception of two custom feedthroughs (Kurt Lesker, Inc.), one in the main chamber and one in the source side. The special feedthrough in the UHV side is a 6 inch con-flat flange that has both copper and water feedthroughs. There are six-1/4 inch diameter copper feedthroughs for current to the wire traps as well as a multi-pin connector, which was included originally for transmitting radiofrequencies through an in-vacuum antenna. This antenna broadcasted to the laser locking electronics, and so we opted for an external rf-coil instead. This unusual behavior was not understood and may not be present anymore because the original Toptica DLX-110 laser has been refurbished (upgraded to a "rock-solid" configuration), which dramatically increased its stability. In addition, we replaced the homemade locking circuitry with a commercial lock box (Precision Photonics).

There is an input and return stainless steel water feedthrough, which is attached to a steel can inside the vacuum. This is intended to help cool the copper block on which the aluminum nitride (AlN) bed for the wire traps (described in Section 2.4) is situated. Good thermal contact between each piece of the assembly is crucial for the traps to be efficiently cooled. We have recently observed that when the cooling and heating of the traps during the experimental duty cycle is extreme, the thermal stress can weaken the mechanical connections and potentially lead to damage (the gold mirror breaking). The structure with the traps extends vertically through a 6 inch flange, 4-way cross into the spherical octagon chamber (photos

shown in Fig. 2.1).

Achieving very low pressures requires care, and is made more difficult by introducing structures into the chamber. All parts of the attachments to the feedthrough, with the exception of the gold-coated wafer and an AlN piece, were cleaned by hand with vacuum grade acetone and Kimwipes®, and using an ultrasonic bath, repeated multiple times. The cleaning of the copper parts included an acid dip made of 3:1 mixture of water/12 M sulfuric acid. Acid type dips are suitable for cleaning OFHC (oxygen-free high conductivity) copper, but caution should be taken for cleaning other materials using this method due to the risk of etching. Vacuum equipment ordered new was not cleaned, since typically these pieces are baked at the factory. All gaskets were wiped with acetone. In an assembly such as ours, where many materials are put under vacuum, gaskets and factory baked equipment are usually not the limiting factors in achieving low pressures. All assembly screws are vented to avoid trapped pockets of gases. Once the system was assembled (in its original configuration without the slower/oven) we roughed out using an adsorption pump until the ion pump could be turned on (typically around 10^{-5} torr). After the pressure lowered to 10^{-8} torr , we wrapped the chamber in heater tape and aluminum foil and baked at just under 150 °C for 1-2 weeks. The limiting factor on the baking temperature is the anti-reflection (AR) coatings on the windows. We take special care not to create any large temperature gradients in the baking process due to the fragile ceramic feedthrough, the coated windows, and the glass science cell (because of the seal, see below). Once we added the Zeeman slower, the baking procedure became more complex. The stainless steel 14 inch long nipple (inside tube that the

slower coils are wound on) is wrapped in heater tape and terminates at the gate valve/differential pumping region. Very recently, upon breaking vacuum it became critical for maintaining low pressures to bake the gate valve area. The maximum temperature for this is 150 °C when the valve is open and 120 °C when it is closed (limitation is the O-ring).

The science chamber is a commercially available 4.5 × 2.2 × 1.2 cm^3 quartz cell. The cell is fused (by the glass blower at NIST, Gaithersburg) to a glass cup that is sealed to a stainless steel 2.75 inch con-flat flange (Bomco). The glass to metal seal on the flange is sensitive to both applied pressure changes and temperature gradients. (When it was first attached to the vacuum, the stress from screw tightening cracked the seal.) Being meticulous paid off, as we had no real difficulty in getting down to 4 $\times 10^{-11}$. After the addition of the source side, the UHV routinely is at 7-8$\times 10^{-11}$ torr. In later instances, we used a turbomolecular pump (Pfeiffer Vacuum)/roughing pump combination for getting to pressures of 10^{-6} Torr, before turning on the ion pump(s).

2.2 Experimental Sequence for Creating a BEC

A typical duty cycle for creating BECs in our experiment is:

- Atomic source
- Collect 10^9 atoms from beam in a MOT
- Optical molasses stage

- Optically pump to trapped state
- Collect atoms in weak magnetic trap
- Compress magnetic trap
- RF evaporation to critical point
- Release atoms and take absorption image

These steps will be discussed in detail in the sections to follow.

2.3 A Source of ^{87}Rb atoms

This section describes the source of atoms we use for forming a condensate. We have had two sources in our experiment: Rb dispensers (getters) and a Zeeman slower. I will first discuss the getters, as that was our original source for rubidium atoms and give some reasoning for why we later implemented a slower.

2.3.1 Getters

The boson we choose to work with is the very popular, ^{87}Rb. It is the less abundant isotope of Rb (27 %). As compared with ^{85}Rb, it has a positive s-wave scattering length, which means that its interactions are repulsive at very low temperatures. It has been shown that condensates with attractive interactions and sufficiently large numbers are unstable and collapse [18]. Rb has a single valence electron so it is easily laser-cooled. Rb is also a good choice because of the com-

mercially available lasers with the required wavelengths. It is also inexpensive to obtain, less than $100/gram.

We originally designed our system to have only a single vacuum chamber. In this configuration, we used Rb alkali dispensers (SAES getters) as the atomic source. Rb dispensers are essentially a tungsten envelope containing Rb bound up in an inorganic compound. Rb is released diffusively from the envelope when current flowing through the getters reaches a value corresponding to a threshold temperature (at around 2.7 amps) required to free the Rb from the compound. The dispensers have been shown to be effective in MOT loading and their turn-on/turn-off properties have been studied [24, 51] . Our system was equipped with two sets of three getters, one arranged in series and one in parallel.

In our set-up, using the dispensers proved troublesome to maintaining the required vacuum pressure. When the getters release Rb into the vacuum, only a fraction is captured by the MOT. The remaining Rb is pumped out by the walls, the ion pump, and other surfaces inside the vacuum (i.e. gold mirror). There is an inherent time constant (on the order of 10 s in our apparatus) associated with this pumping. In addition, one must gently warm the getters just below threshold current in order to maintain their cleanliness.

The release of Rb from the getters as a function of current is exponential. After initially achieving BEC, during the optimization process, we accidentally released too much Rb into the system which subsequently formed an alloy with the gold mirror, requiring its replacement. In order to prevent destroying the mirror, we built an electronic interlock system to shut-off current to the getters. We placed a

resistor in series with the output of the power supply and measured the temperature of the resistor with an AD590 (Analog Devices) sensor. An AD590 is a chip that has an output of 1 μA/°K. After a few experimental duty cycles, the resistor temperature reaches a steady state value. If the temperature of the resistor exceeds this value, the supply is shut-off. After achieving BEC, we spent approximately 6 months trying to optimize the duty cycle for the getters and eventually concluded that this type of source did not lead to stable operating conditions conducive to doing reliable experiments. The use of the single-chamber getter-based system was based on [67]. We believe that our difficulties were probably due to differences in chamber/pump geometries. At their best operation, we ran the getters in pulsed mode, with a cooling/pumping stage prior to loading the magnetic trap, leading to a total MOT loading phase of 20 s. During this process, we began to design a substitute source. Currently there are getters in the vacuum, which serve as a tool to implement an electric field. However, they are not connected to operate in dispensing mode.

2.3.2 Rubidium Oven

Rubidium is a solid at room temperature with a boiling point of 688 °C and a melting point of 39.3 °C. Our atomic beam is designed to be a crude version of the candlestick source [63]. After breaking an argon-packed Rb ampoule (Strem Chemical) under vacuum by bending a bellows (Kurt Lesker Inc.), we heat it to 105 °C. The temperature is achieved by wrapping heater tape around the bellows and the stainless steel "T" housing the collimator. The oven region is wrapped in

sheet copper, insulating fiberglass material, and aluminum foil. The temperature is measured by a thermocouple and maintained by a servo-controller (Omega).

The diffusive beam is approximately collimated by custom machined copper apertures. In practice, this acts more as a nozzle, and un-collimated Rb mostly sticks to a cold-plate. The atoms that do not enter the source chamber (spherical square, Kimball Physics Inc.) are ideally recycled by a gold mesh via capillary action and returned to the Rb reservoir. The cold plate is cooled far below the melting point by an external TEC cooler clamped to a 3/4 inch copper feedthrough. The TEC is maintaining a large temperature gradient and has one side water cooled for efficient heat dissipation. When the water cooling stops the TEC cannot maintain constant cooling of the copper block and the heat from the back of the TEC will heat the copper cold plate. Since Rb tends to drastically shorten the lifetime of ion pumps, this cold plate also serves as a preventative measure. Even with these measures, the failure of the cold plate TEC cooler will lead to catastrophic poisoning of the source side ion pump. As another measure, we heat the ion pump above the melting point of Rb in attempt to prevent it from sticking to the walls. A Rb contaminated pump exhibits high leakage current and eventually a high base pressure. (We keep a spare 30 L/s ion pump and when this damage occurs, we send the contaminated pump for refurbishing). In short, it is critical to keep the Rb localized and away from the ion pump or it will contaminate everything.

A schematic of the source side plus the Zeeman slower is shown in Fig. 2.2. The pressure on the source side is maintained at two to three orders of magnitude above the UHV side by a 30 L/s Varian-type pump (option diode or triode, Duniway

Stockroom). This is sufficient to maintain a 10^{-8} Torr vacuum. The pressure on this side is naturally higher due to the rubidium (Rb) oven. Separating the two sides is a differential pumping section which is simply an aluminum tube of 8 cm in length and 3/8 inches diameter. The desired dimensions of the tube were determined by calculating the conductance. (Conductance is the inverse resistance of flow from one location to another.) Other than preserving vacuum with a cold plate, separating the two chambers is a manual gate valve (Kurt Lesker, Inc.). Adjacent to the differential pumping stage we use a rotating ball-valve, which opens every experimental duty cycle to allow the atomic beam to pass into the slower and UHV chamber. This ball valve serves to quickly reduce the conductance of Rb between the source and UHV chambers. It is affixed to an aluminum rod which screws into a custom feedthrough (Kurt Lesker Inc.) next to the 3/4 inch copper feedthrough. The ball valve is rotated via a magnetic rotary feedthrough (magidrive, Kurt Lesker Inc.). Externally, the rotary feedthrough is attached to a stepper motor which is given $\pm$ 5 V to "open" and "close," respectively.

2.3.3 Zeeman Slower

There are two main alternative sources to getters: a double-magneto-optical-trap (double-MOT) system and a Zeeman slower. Our associations at the "birth-place of the slower," NIST, led us to choose the latter. This choice also proved relatively convenient to implement. A brief description of the theory of a slower is given here.

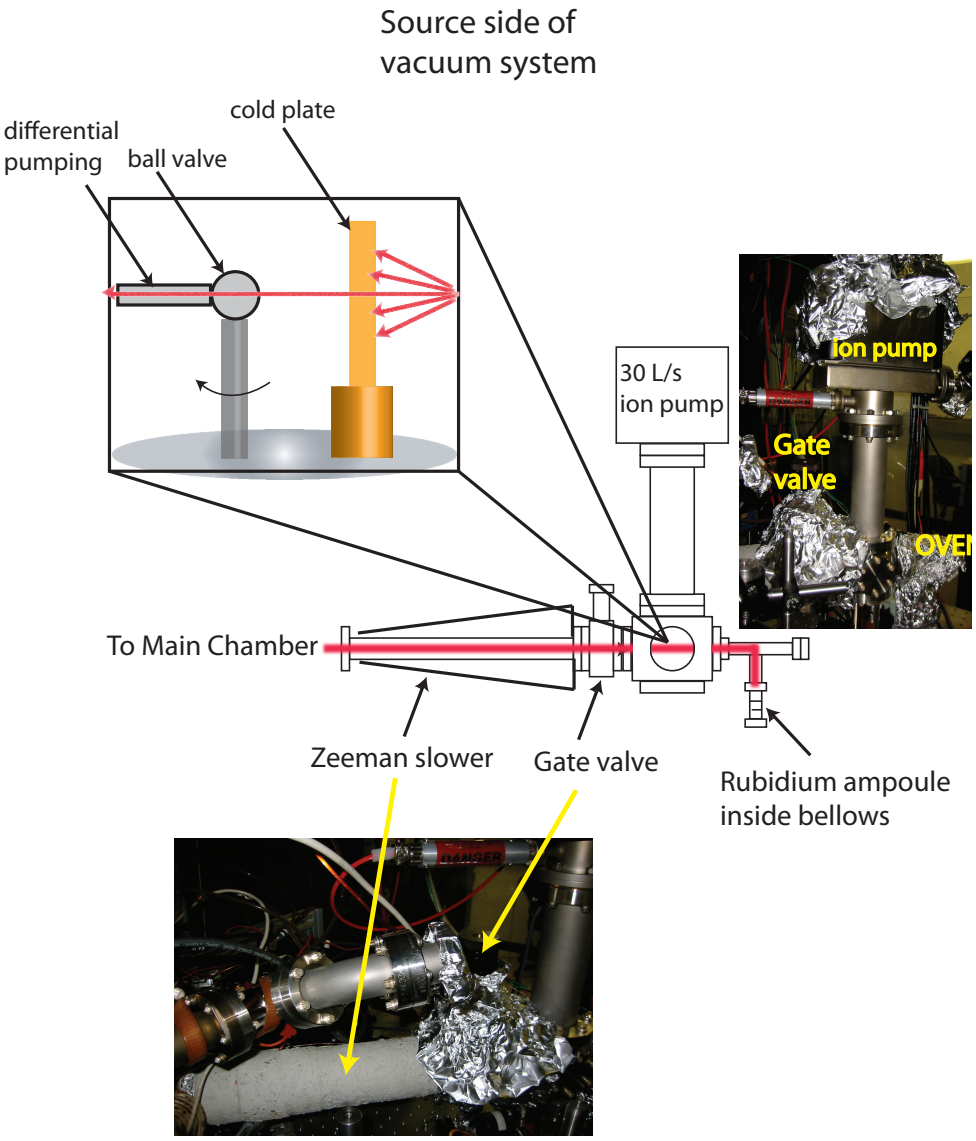

Figure 2.2: Layout of source side of the vacuum system with photos of the apparatus.

A slower uses the combination of two techniques to create a low temperature, low velocity atomic beam: laser-cooling and the Zeeman shift. For a detailed description of these ideas, see [42]. If an atom is traveling in a given direction and absorbs a resonant photon from the direction opposite to its propagation it acquires a momentum kick, $-\hbar k$, where k is the wavevector of the photon. Upon relaxation, the atom releases a photon, but as the spontaneous emission can statistically be in any direction, the momentum transfer to the atoms from this process averages to zero. The net momentum transfer is then $-\hbar k$. Following many cycles of the absorption-emission process, one can imagine that the atomic velocity decreases. If one applies this technique to a beam of atoms, one can essentially stop the sample motion in the direction of propagation. The maximum deceleration of an atomic beam is $a_{max} = \hbar k\gamma/2M$, where M is the mass and γ is the natural linewidth of the transition which is 6 MHz for the D2 line of Rb. In the case of ^{87}Rb, a_{max} is $0.113 \times 10^6\ m/s^2$ (line data information from [62]).

Due to the distribution of the velocities of atoms in a collimated beam,

$$f(v_z) = \left(\frac{v_z^3}{2(k_bT/M)^2}\right) e^{\frac{-v_z^2}{2(k_bT/M)}}, \tag{2.1}$$

compared with the narrow linewidth of the laser, only a fraction are in resonance with the photons. Here, T is temperature and v_z is the velocity along the atomic beam direction. As the atoms are slowed, the Doppler shift, $\omega_D = -k \cdot v_z$, pushes them out of resonance, which makes repeated absorption-emission cycles unlikely. For ^{87}Rb at 100 °C, v_{rms} is approximately 360 m/s and $\omega_D \approx$ -480 MHz. Each absorption-emission cycle slows the atom by $\hbar k/m = 0.6$ cm/s, which is an $\omega_D \approx$ -

7 kHz. After about 800 cycles, the atoms are shifted by a linewidth. Fortunately, there are ways to compensate for the Doppler shift, such as continuously changing the laser frequency in time or shifting the atoms into resonance using a magnetic field. These methods allow a significant portion of the atomic beam to be cooled and slowed. We choose the latter of these techniques because chirping the laser frequency produces a pulsed source of slow, cool atoms and we desire a continuous beam.

The hyperfine splitting due to the coupling of the nuclear angular momentum ($I = 3/2$ for ^{87}Rb) with the total angular momentum of the electron, J, has degenerate sub-levels. These levels (m_F) are split in the presence of a magnetic field. In a weak field, this phenomena is the Zeeman effect and the shift of the levels is $\mu_B m_F g_F B$, where μ_B is the Bohr magneton and g_F is the g-factor. A Zeeman slower uses the magnetic field dependence of the the levels to maintain resonance between the slowing atoms and the laser beam. To keep a constant deceleration, the parameters must satisfy the condition $\omega_D + \mu B/\hbar = \Delta$, where $\Delta = \omega_{laser} - \omega_0$ is the detuning of the laser from atomic resonance (ω_0). Using the relationship $v_f^2 = v_i^2 - 2az$, one finds that the optimal field profile for slowing an atomic beam is $B(z) = B_0\sqrt{1 - z/z_0}$, where z is along the axis of the atomic beam. Decreasing the rms spread in velocity corresponds to lowering the temperature (i.e. deflection or deceleration is not cooling). Note, that in the decelerating atom frame, Zeeman slowing looks like typical laser cooling [42]. Although strictly speaking, temperature is not a good description because the atomic beam is not exchanging heat with its surroundings, and thus is not coming to thermal equilibrium.

Our slower was originally configured to be a "reverse" or σ^- slower meaning that the atomic beam enters the slower at a point where the magnitude of the field starts small and increases down the length. The advantage of a σ^- slower over a "traditional" σ^+ slower is that the laser frequency is not resonant with the low velocity atoms exiting the slower [5]. Many slowers have a σ^- and σ^+ portion, which combines features from both types. Because table space was limited and this was an add-on to the original design, we opted for the σ^- slower. The optimum slower laser detuning is set according to where the magnitude of the field is at a maximum. In practice our reverse slowing technique did not work very well, so we adjusted the currents to form a field profile optimum for a "$\sigma^+ - \sigma^-$" slower, which as a zero-crossing in the field profile. The laser detuning, fixed by the value of the field at the end of the slower, is aligned to pass through the MOT and focus on the oven aperture. Because resonant light would push the MOT around as it was loaded, the detuning of the slower frequency is chosen to be many linewidths off-resonant ($\sim$110 MHz). The final coil in the solenoid provides compensation for the slower field so that there is not a significant gradient at the MOT.

The solenoid consists of 7 individual solenoids to allow us to easily modify the field profile by adjusting each of the coil currents. A linear supply is used to drive the current in the coils. There is a circuit which divides the current and farms it out to each individual coil (Fig. 2.3). The coils are wound with 14 AWG kapton-coated flat, copper wire. Even though our slower is quite short, we still get a reasonable flux of atoms. Due to our "mirror-MOT" plus Z-trap configuration (see MOT and Z-trap sections) our capture volume is smaller than more traditional traps, thus we

do not require large numbers of atoms. In practice we load 0.5-1 $\times 10^9$ atoms into our MOT in 5 seconds of slowing. This is compared with 3D MOTs which typically capture $> 10^{10}$ atoms.

2.4 Trapping atoms: Lasers and Magnetic Fields

Once there is a reliable source of atoms in a high vacuum environment, one requires a method to capture them in free space. There are two main techniques to do this: Magnetic fields and optical fields. The combination of near resonant laser light and magnetic fields gives rise to the very popular magneto-optical-trap or MOT. In this section I will discuss the MOT and the purely magnetic trap as these are the methods used in the formation of the condensate. In a later section about optical lattices, I will describe the features of optical traps.

2.4.1 Magneto-optical trap (MOT) and optical molasses

The MOT [50], one of the most powerful tools in experimental cold-atom physics is a combination magnetic and optical fields to create a trap for neutral atoms [42]. Our Zeeman slower used laser cooling in one direction. In principle, one could cool in all three directions, potentially creating a ball of atoms instead of a slow moving beam in primarily one direction. Suppose one has two counter-propogating beams with oppositely circular polarized light relative to one another. An atom moving from the center of the overlap region will preferentially undergo multiple scattering events with the beam moving opposite to its direction of motion

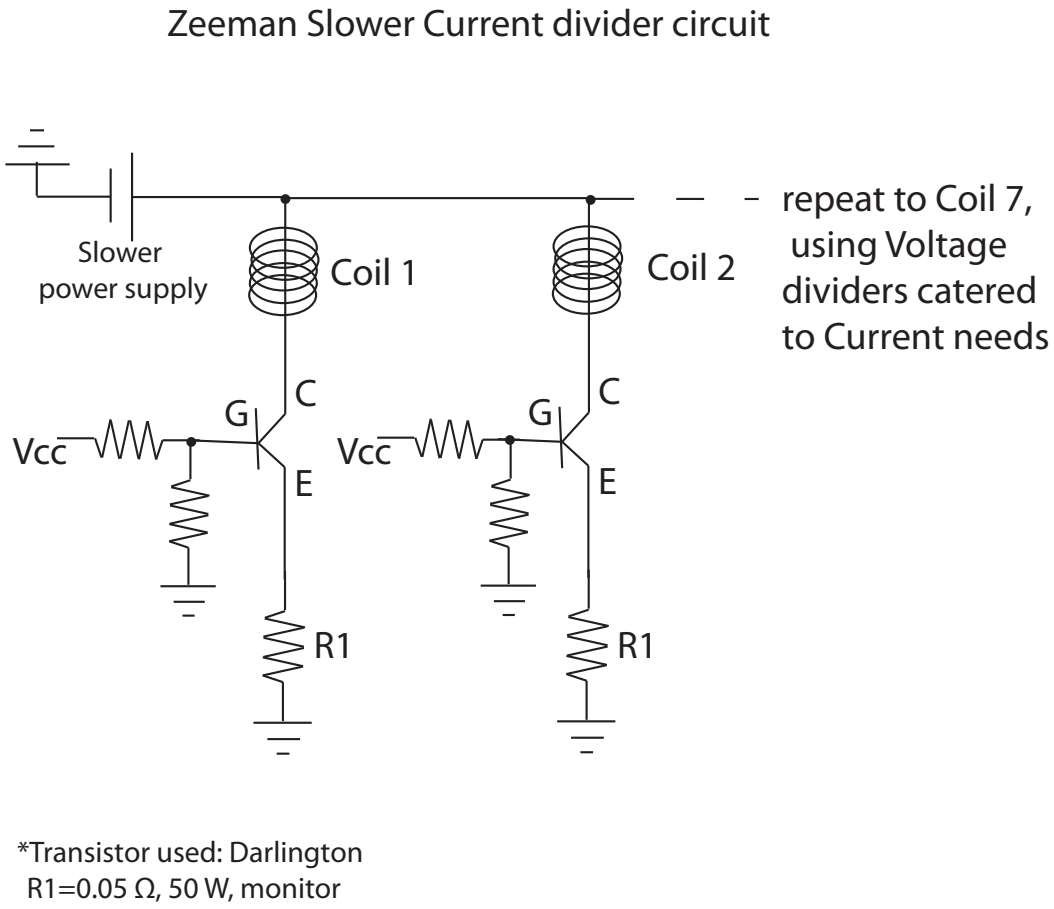

Figure 2.3: Circuit schematic for driving current in the Zeeman slower coils.

because the light will be Doppler shifted towards resonance. As with the case of the Zeeman slower laser beam, the atom will be pushed. At some point it will see more resonant photons from the other beam. This situation in three directions will create a viscous damping of atoms at the overlap region, and is known as optical molasses. This is not a trap, because an atom moving at non-zero velocity, but displaced from the center of the overlap region, will not feel a force pushing it towards the middle.

A quadrupole configuration produces a field which increases in all directions and has a zero at the center. The interaction of the atoms with the field, through the Zeeman shift, provides a spatially dependent scattering rate resulting in the restoring force necessary to create the trapping conditions. The combination of these two techniques creates a harmonic trap (for small displacements) with damping, where a large sample of atoms can be collected and continuously cooled. A schematic representation of our MOT geometry and laser beams is shown in Fig. 2.5.

In the science side of the vacuum there are two wire traps: the U-trap and the Z-trap. This type of design has become quite popular in the form of micro-fabricated atom chips. We modeled our design after [67]. The U-trap is used in conjuction with external coils to form a quadrupole field profile for the MOT. A schematic and picture of this is shown in Fig. 2.4. If one examines a thin current-carrying wire, the field decreases as $1/r$. Adding a bias field, B_{Bias}, perpendicular to the wire will cancel the field due to the wire, thus creating a field minimum at a specific distance in one direction. Along the line parallel to the wire, the field is a minimum, but bending the leads to form a "U" adds a gradient in this direction as well, creating a three-dimensional trap. In the case of the U-trap, the field lines are at an angle

with respect to the idealized quadrupole and so to avoid this, the middle wire is flattened into a plate [67].

We employ a mirror-MOT which is a modification of the traditional six-beam MOT [52]. There is an in-vacuum gold-coated silicon wafer situated on top of the wire-traps. Two beams enter the bottom window of the chamber and reflect from this mirror at an angle. There are two additional beams counter-propagating, which enter the chamber from side ports. The combination of these laser fields provides the 3D laser cooling in the MOT (Fig. 2.5) since the beams reflecting off of the mirror overlap with the capture area prior to and after their reflections. The MOT beams are detuned from resonance by approximately 20 MHz. This value was determined empirically by optimizing atom number.

After up to 10^9 atoms are loaded into the MOT in 5-7 s, a second cooling stage called optical molasses follows. The name molasses refers to the viscosity of the light field (as described above and in Ref. [9]). The technique is simple: abruptly turn off all magnetic fields. The atoms are very cold in the MOT and in zero-field, they will take some time to move out of the region of interest. Additionally, we reduce the radiation pressure pushing outwards (force due to re-scattering photons) on the atom cloud by lowering the intensity of the light fields and detuning several linewidths away from resonance. This stage cools the atoms to 30-40 μK. The process is necessary for efficient transfer to the purely magnetic trap (Z-trap), whose depth is $\sim$mK. This step has been optimized to take a few ms. At times longer than a few ms, atoms move away from the overlap region with the magnetic trap. Additionally, the temperature at 10 ms is not measurably cooler than at 5 ms. We extract the

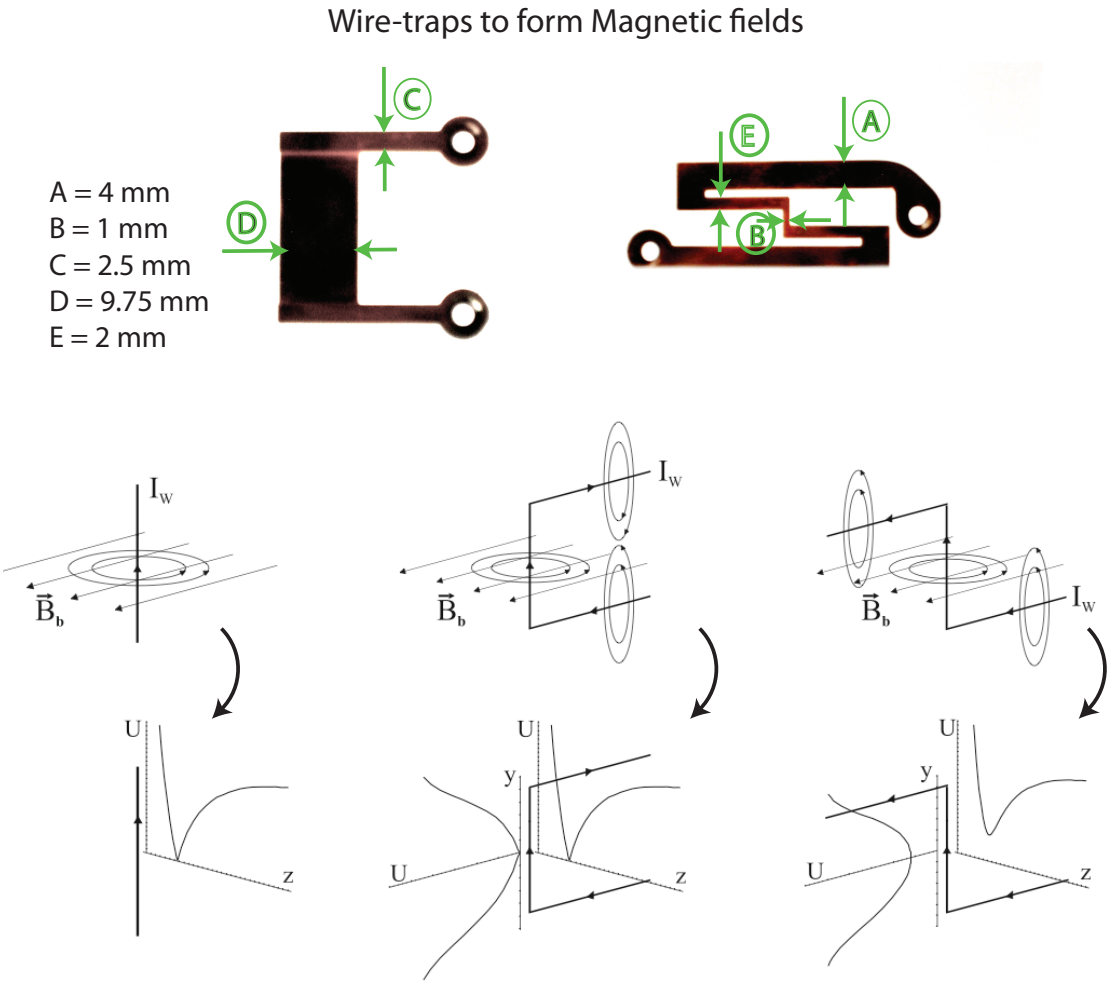

Figure 2.4: Diagram depicting how magnetic traps can be formed from bending wires. B_b is a uniform bias field created by external coils (see Ref. [67]). The dimensions of the wires used in our experiment are shown on pictures of the traps.

temperature (in each direction, x and y) of the molasses by measuring the widths of the atomic cloud (via absorption imaging, see Section 2.8), $\sigma_{x,y}$, after different expansion times, t_1 and t_2, using

$$T_i = \frac{(\sigma_{2,i}^2 - \sigma_{1,i}^2)m}{k_B(t_2^2 - t_1^2)} \tag{2.2}$$

Here, M is the mass of ^{87}Rb and i is a direction, x or y. This equation assumes the equipartition theorem in one-dimension, $\frac{1}{2}Mv_i^2 = \frac{1}{2}k_bT_i$ [65].

2.4.2 Optical pumping

The atoms in the MOT are in a nearly equal distribution of $|m_f\rangle$ states of the $|F = 2\rangle$ ground state. There are $2F + 1$ sub-levels of this state. Only the low-field seeking states are capable of being confined by the magnetic trap. At low fields the possible states are $|F = 2, m_F = 2\rangle$, $|F = 2, m_F = 1\rangle$, and $|F = 1, m_F = -1\rangle$ of the $5^2S_{1/2}$ level. We choose the $|F = 2, m_F = 2\rangle$ state and the atoms must be transferred to this state. Presumably, doing this with 100% efficiency would yield a factor of 5 increase in number of trapped atoms over not having this step. In practice, we observe a factor of 3-4 in atom number and is probably limited due to imperfect polarization. We optically pump using σ^+ polarized light (defined along the quantization axis of the magnetic trap, which is in the B_y direction) resonant with the $5^2S_{1/2}|F = 2\rangle$ to $5^2P_{3/2}|F' = 2\rangle$ transition. According to the selection rules for this transition, once the atoms are in the $|F = 2, m_f = 2\rangle$ state the light cannot transfer them to another sub-level. The power and width of the optical pumping pulse must be optimized for best results. We find that the optimum time and

power to maximize the factor of increase in number of atoms captured from optical pumping, but minimize heating, is less than 500 μs and 0.5 mW, respectively (for a $\sim$1 cm size beam).

2.4.3 Magnetic confinement in a Ioffe-Pritchard type trap: Z-trap

At the minimum of a quadrupole field profile, there is a zero in the field and atoms can be potentially lost from the trap by spin flipping (Majorana losses). However, if the Larmor precession rate is much faster than relative changes in the field during an atoms' orbital motion, then this is not a problem. When a large fraction of the atoms occupy low-lying levels (e.g. due to strong cooling), then the condition for adiabatic following is not satisfied. Thus, this loss mechanism is a concern in the evaporative cooling regime near the condensation transition [42].

To avoid Majorana losses, the atoms must be confined to a non-zero B-field. There are three major methods to accomplish this: an optical plug at the zero, a time-orbiting potential which moves the zero, or a Ioffe-Pritchard trap which is designed to remove the zero with an offset bias field. In our experiment, a Z-shaped wire provides the necessary fields to produce a the Ioffe trap (Fig. 2.4). Starting with the central bar, the current flowing through it yields a field that falls off as $1/r$. The external B_x-field serves to cancel the field, creating a magnetic field minimum, which is zero along the bar . However, the leads on each side (now bent into a Z-shape) shift the minimum from zero, to prevent Majorana spin flips. This combination by itself is enough to create a magnetic trap, however, we add a component, B_y in order

to increase depth and field gradient. Our trap has a depth of around 1 mK and a gradient (when compressed) of approximately 400 G/cm (for details about coils, see Section 2.4.4) . The trap is anisotropic with a weak direction along the middle bar of the wire. A diagnostic program calculating the parameters of the magnetic trap was written by M. Beeler.

Physically, the Z-trap is situated on top of the U-trap, separated by a thin layer of Kapton® film (McMaster-Carr), and embedded into an aluminum nitride, AlN, substrate (Stratamet). This substrate was chosen due to its high thermal conductivity of 175 W/mK compared with ceramic (29.3 W/mK). It is a soapy material so care must be taken to isolate it from water.

Following the optical pumping pulse, we simultaneously ramp on the three required fields for the Ioffe-trap in 5-10 ms. The initial currents were chosen to match the trap with the position of the molasses cloud. The initial trapping frequencies are approximately $\omega_{ho} = 2\pi \times 20$ Hz. The trap is immediately compressed during 250 ms to frequencies $\omega_{x,y,z} = 2\pi \times (410, 120, 410)$ Hz. The frequencies are measured by abruptly changing the magnetic field, which induces oscillations of the atomic cloud in the trap. The frequencies are extracted by varying the hold time following the perturbation of the system. This method works well for the compressed cloud after some evaporation. However, it cannot be used for the initial trap because of the large extent of the cloud compared with the image area. Therefore, we use a magnetic field calculation to determine these values. They are not critical because all experiments are performed in traps that have been compressed and characterized.

This compression step serves to dramatically increase the collision rate, $n\sigma v$.

Here, n is the density, σ is the s-wave scattering cross-section, and v is the thermal velocity. This collision rate determines the rethermalization time after each step in evaporative cooling, thus it is necessary to start with a high density of atoms. In our system, compression also moves the trap closer to the wires/mirror because higher frequencies are attained by approximate cancellation of the field at the wire.

There is noise which couples to the magnetic trap and heats the atoms. This heating is trap bias dependent which suggests that it is rf noise. We have not discovered the source of this noise and avoid it by changing the trapping parameters prior to or after achieving BEC, depending on the application. It appears that traps with a bias above 6-7 MHz heat at a rate of 10-100 nK/s compared to rates of 1-2 μK/s in the lower bias/higher [trapping] frequency traps.

Additionally, for experiments where one decompresses the magnetic confinement, the trapping frequencies pass through 60 Hz and harmonics. This will drive oscillations which will add position noise on the sample. To minimize this effect, we abruptly pass through these resonances in a time step chosen to be faster than the response of the atoms.

2.4.4 Coils: Bias and trimming fields

All coils in our system are external to the vacuum and are for creating effectively uniform fields at the location of the atoms. There are three main coils, B_x, B_y, B_z (see Fig. 2.5 for orientation). Both B_x and B_y are made of rectangular, hollow copper tubing that are water cooled. The tube dimensions, including coating

are 4.4 × 4.5 mm^2. The coils for B_x are insulated with a fiber-glass type coating (tan-colored) and are comprised of two coils, each 42 turns (6 rows of 7 turns), situated around a 2 3/4 con-flat flange on each side of the vacuum chamber. The B_y coils are kapton® film coated (orange-colored), also water cooled with each coil having 35 turns (5 rows of 7 turns) and oriented perpendicular in the plane with respect to B_x. In the original configuration we used air-cooled coils for creating the B_y field. After many duty cycles they would come to thermal equilibrium, however this process took many hours. We attempted to add heat sinks to the coils, but this did little to improve the time constant. For this reason, they were replaced with water-cooled copper tubing. The B_z coil is situated around the bottom window of the chamber (6 inch con-flat flange), and has 25 turns (1 row, 25 turns) of 20 AWG kapton® coated wire (magnet wire, air-cooled).

We have wound "trim" coils onto the chamber due to residual fields and for finely tuning the fields at the location of the atoms during different stages, such as optical molasses. These consist of a few turns (4-6) of 20 AWG magnet wire wound around the conflat flanges in x, y, and $slower - beam$ directions. The trim coils are fixed to the chamber with epoxy.

2.4.5 Circuitry and power supplies

We use Sorensen DLM-600 power supplies to run up to 75 A of current through our wire traps and water-cooled wires. There is an interlock which prevents the user from running the supplies when there is no flow in the coils and/or chamber. The

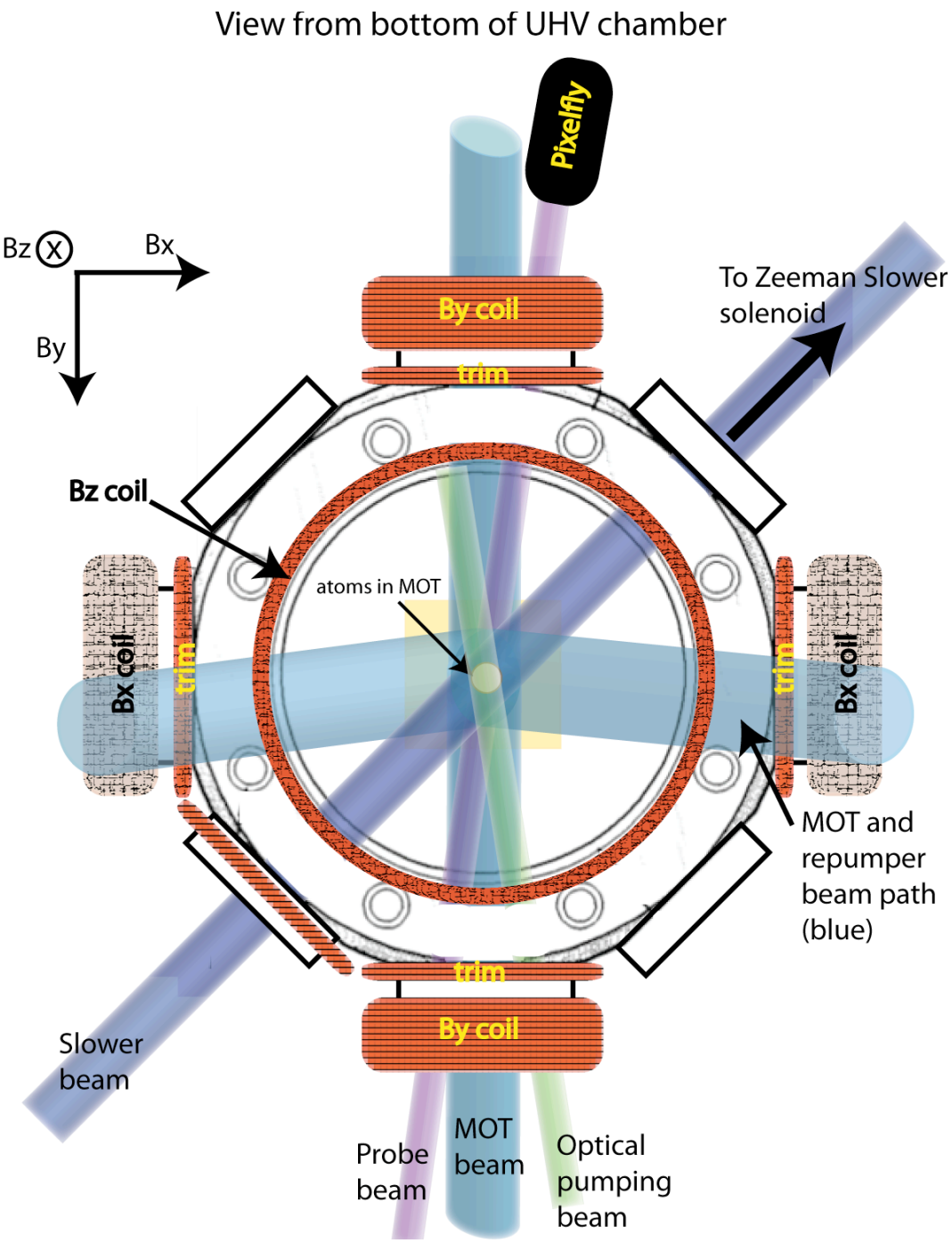

Figure 2.5: View from the bottom of the UHV chamber showing coil orientation and input beams for MOT. There are four beams total, two from the side and two from the bottom. The reflection off the gold mirror gives the other two required beams for 3-D cooling in the MOT.

water pressure directly from the laboratory source is too low to be useful so we installed a booster pump (McMaster-Carr) to bring it up to 100 psi. The water is conveyed to the necessary places in the experiment by hoses. A flowmeter on the output of the booster pump outputs a voltage proportional to the water flow. This voltage is compared to a set point and when there is no flow, the circuit sends a voltage to the rear connector of the supply which disables the output. The B_z coil is powered by a Sorenson XLT-60 supply.

Typical turn on and off times for the supplies driving the inductive load of our coils is 5 ms and 10 ms , respectively. For our purposes the turn on time is less important as we slowly ramp on the fields over the course of 25 ms. The supply limited turn-off times are insufficient because we require abrupt shut-off of our magnetic fields for sudden release without imparting velocity to the atomic sample. For this reason, we use insulated gate bipolar transistors (IGBT) to switch the current on and off. These transistors were chosen due to their high current carrying capacity. With our relatively low currents compared with typical magnetic trapping schemes which use a few hundred amperes, one could also implement a high powered MOSFET. The IGBTs require a driver circuit to supply high current to the gate to open the switch. The circuit diagram for these transistors is shown in Fig. 2.6.

Because of the inductive load the abrupt shut-off can cause large voltage transients which potentially affect other electronics in the experiment and specifically will damage the IGBT and IGBT driver circuitry. As a precaution we have varistors (see Fig. 2.6) across the load and protection diodes across the collector-emitter of

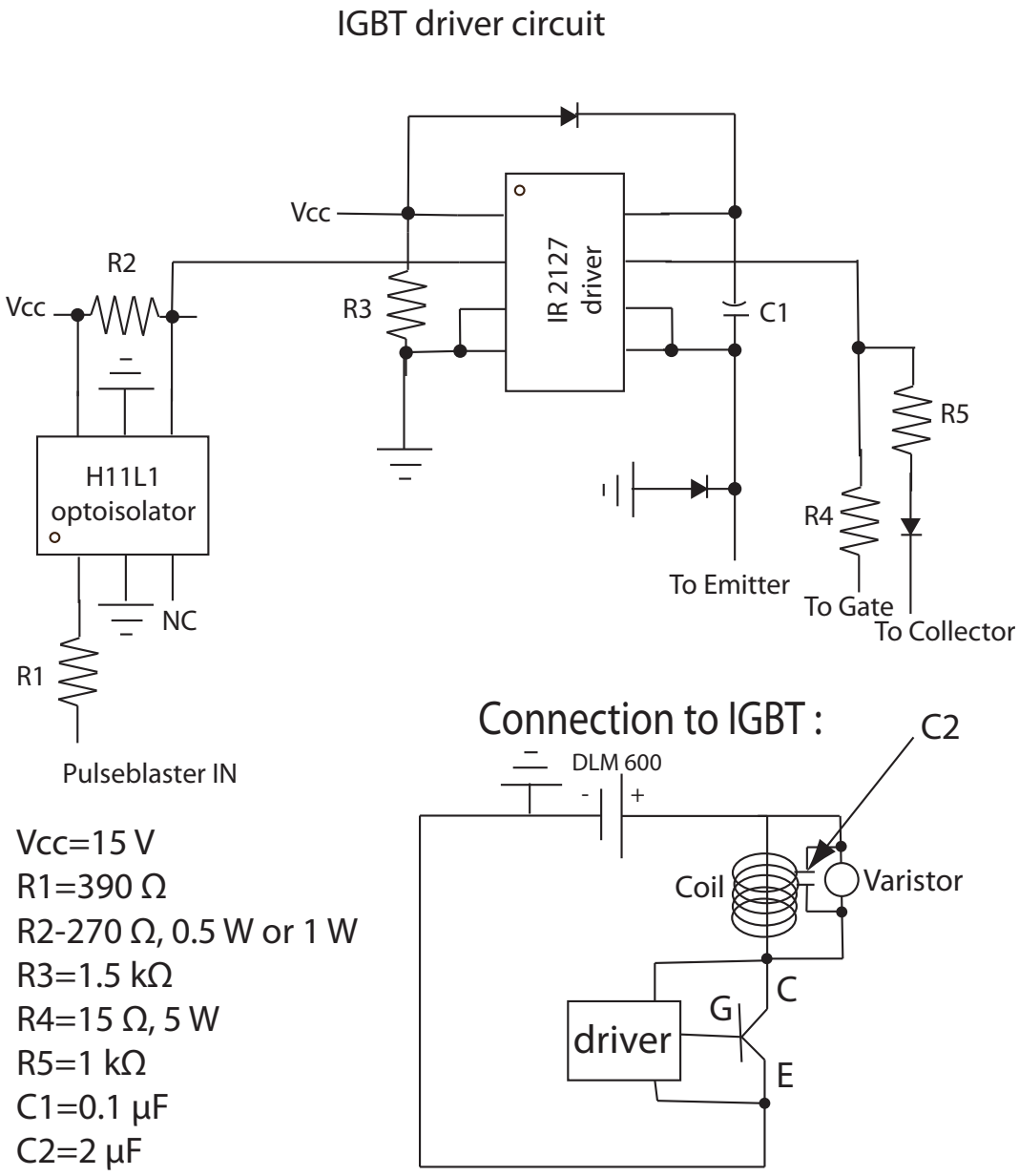

Figure 2.6: Driver circuit schematic.

each transistor. Both of these elements are crucial. We also have an optoisolator preceding the driver to prevent large voltages making their way to the computer control boards. Optoisolators create an electrical break. We monitor the current in each of the magnetic trapping coils (B_x, B_y, Z-trap) using transducers (Danfysik). The devices have a 100 kHz bandwidth and so are not suitable for examining short transients. Measured with these monitors, the coils turn off times are 100 μs or less, depending on individual inductances. We have put capacitors in parallel with the varistors in attempt to reduce ringing when the current is shut-off.

We use Kepco power supplies to run a maximum of 10 amps through each set of trim coils. The value of the current was determined experimentally by measuring the atom temperature of the optical molasses stage.

2.4.6 Lasers

We use semiconductor diode lasers for all applications related to forming a BEC. Other lasers used in this experiment are a Ti-Sapphire laser (Tekhnoscan Laser System) which outputs 1 W of tunable 800 nm light when pumped by a 10 W 532 nm laser (Coherent Verdi). This laser is used to form the optical lattices. We also have a single frequency 15 W 1563.8 nm fiber laser (IPG photonics) for the dipole trap.

Our MOT, optical pumping, Zeeman slower, and probe beams are derived from a 750 mW diode laser (DLX-110 Toptica Photonics). For these applications we require a narrow laser lock so we use phase-modulation on a saturated absorption

spectroscopy set-up which is similar to Pound-Drever-Hall lock [7]. The signal does not come from a cavity reflection, but from an absorption cell. In short, a pick-off beam is shifted to the $|F = 2\rangle$ to $|F = 3\rangle$ resonance using a double-pass 80 MHz acousto-optical modulator (AOM) (Isomet, Intraaction) set-up. A double-pass scheme is generally preferable to decrease beam steering when the driving frequency of the AOM is scanned. The output of the double-pass is split by a beam splitter and one arm is modulated at 14 MHz by an electro-optic modulator (EOM) (New Focus). This EOM puts sidebands on the laser that are 180° out-of-phase with each other. The modulated beam is sent through a Rb cell and when scanned through resonance, excites atoms. The unmodulated beam counter-propogates and burns a hole in the Doppler-broadened absorption signal of the probe beam detected with a photodiode. Without the EOM in place, this is saturated absorption spectroscopy. With the additional phase modulation, the individual sidebands individually interfere with the non-modulated pump beam to give a non-zero intensity modulation at the beat frequency which increases or decreases away from the zero depending on the relative phase. This signal has a zero-crossing which can be used for feedback to the laser.

We also use single and double-pass schemes to generate the desired frequencies for the MOT, optical pumping, Zeeman slower, and probe beams. The magnitude of the shift is dependent on the required atomic transition (Fig. 2.7). A diagram of the optical table, separated into three parts, is shown in Fig. 2.8 (repumper laser), Fig. 2.9 (trap laser, MOT light, optical pumping), and Fig. 2.10 (slower, probe, and slower repumper).

The repumper beam, which is tuned 6.8 GHz away from the trapping light

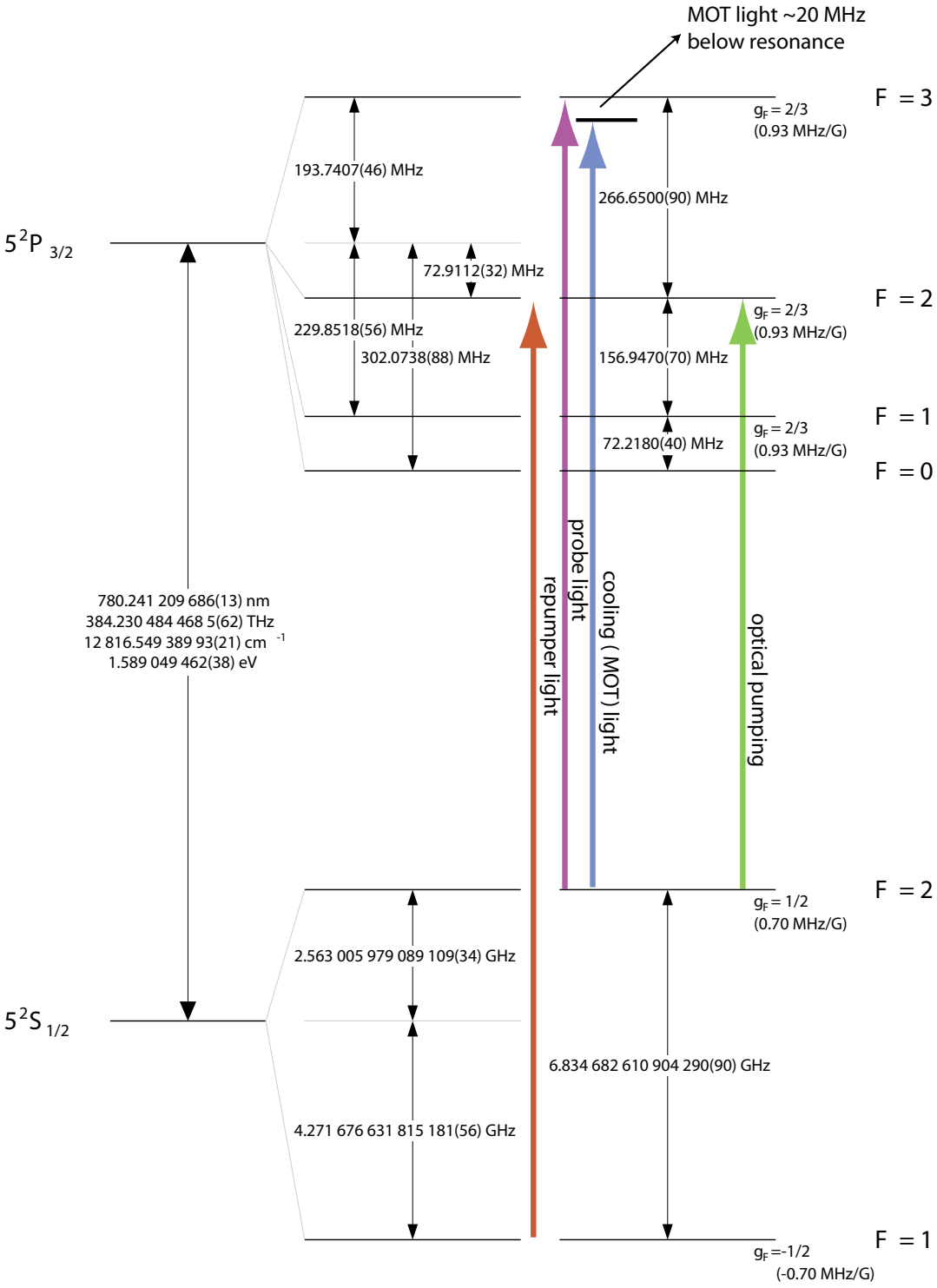

Figure 2.7: D2 line for ^{87}Rb with transitions relevant to our experiment labeled. Underlying diagram and spectroscopy from Ref. [62].

to the $5^2S_{1/2}|F = 1\rangle$ to $5^2P_{3/2}|F = 2\rangle$ atomic transition, does not have strict requirements and so we use a dichroic atomic vapor laser locking (DAVLL) solution [10]. If a resonant laser beam is traveling through a sample of identical atoms, one can in principle observe the linewidth of the transition because of the absorption of photons. Since the atoms are moving with a distribution of velocities given by their temperature, the distributed Doppler shift will broaden this absorption profile. Other mechanisms can cause broadening; for a complete description of spectroscopy techniques see Ref. [15]. This broadened feature can be positively or negatively offset in frequency by magnetic fields if the incoming light is σ^+ or σ^- polarized, respectively. There is magnetic stripping cut into squares on each side of the cell to provide the field. The output of the cell is split into two according to polarization and subtracted (Nirvana detector, New Focus). The subtracted signal provides an error signal for feedback to the laser. This scheme has the advantage of having a large capture range, and not requiring modulation. We temperature stabilize the cell and magnets because long term drift due to ambient fluctuations leads to drift in the lock. A diagram of the set-up is shown in Fig. 2.8. The repumper beam is coupled into the custom 4×4 fiber splitter (Canadian Inst.) and exits along only two of the four outputs. It enters the chamber along the same path as the two MOT beams entering through the bottom window (See Fig. 2.5).

There is a pick-off beam in the repumper configuration for saturated absorption spectroscopy. This serves as a reference for the user, but is not used for locking the laser.

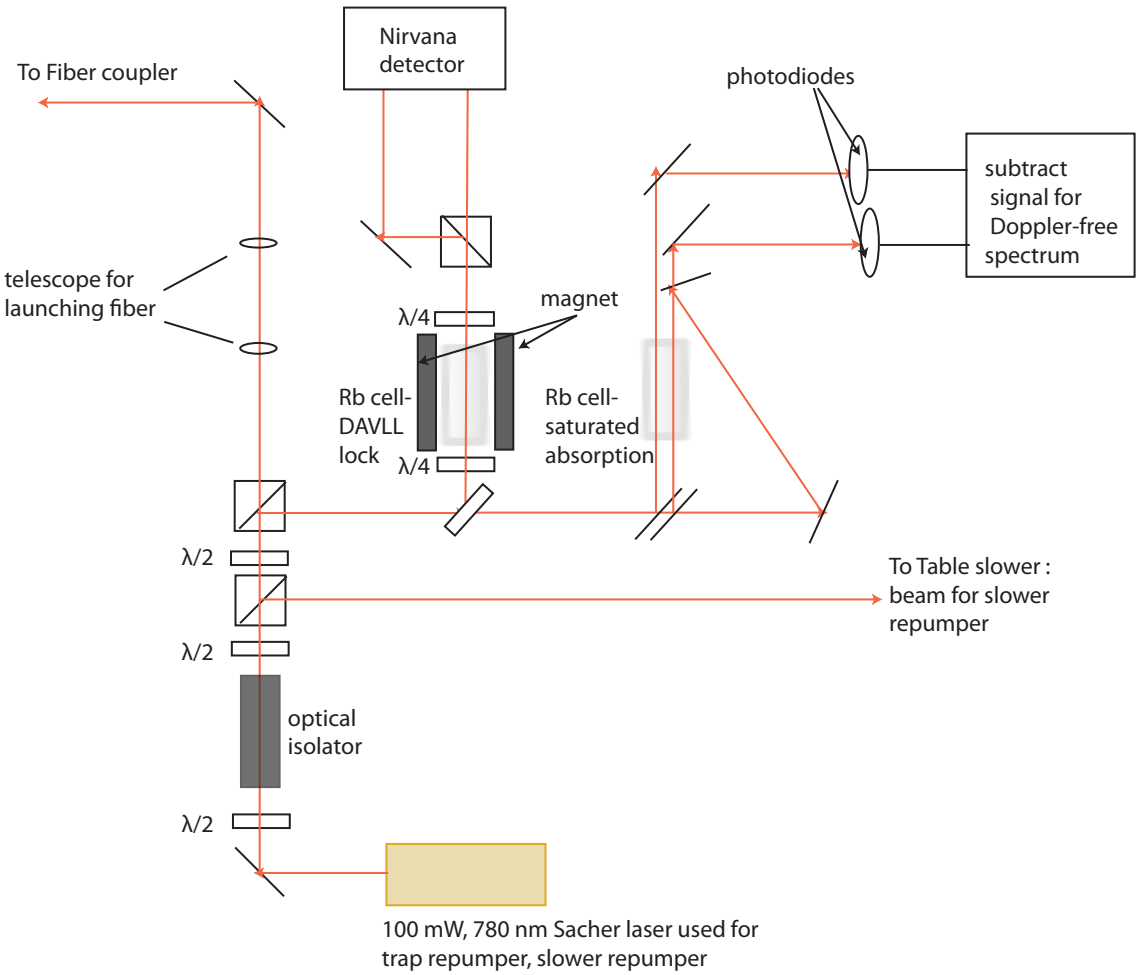

Figure 2.8: Diagram of layout on optical table for the repumper lock and necessary beams.

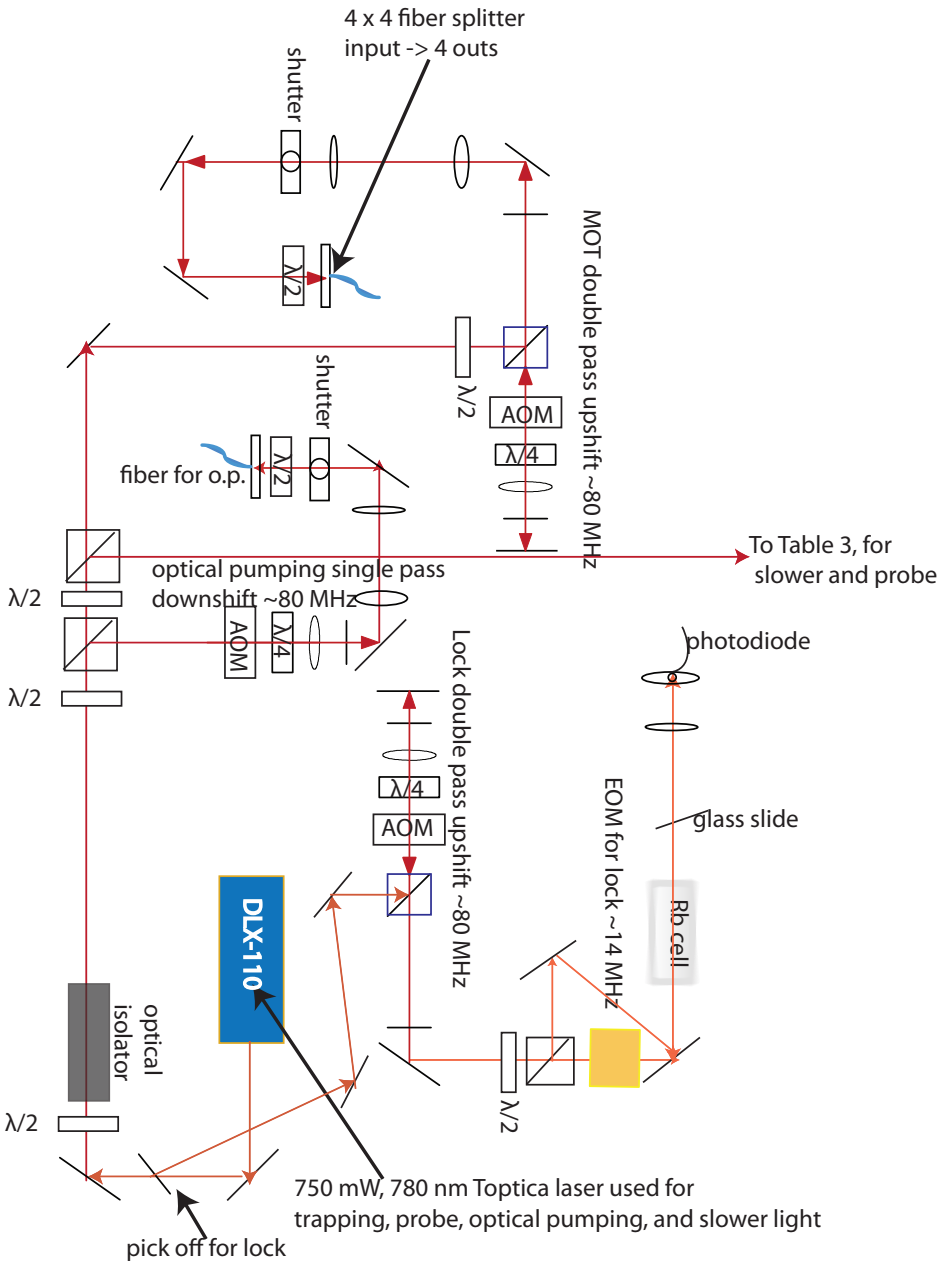

Figure 2.9: Diagram of layout on optical table for the trapping laser, Pound-Drever lock, and necessary beams.

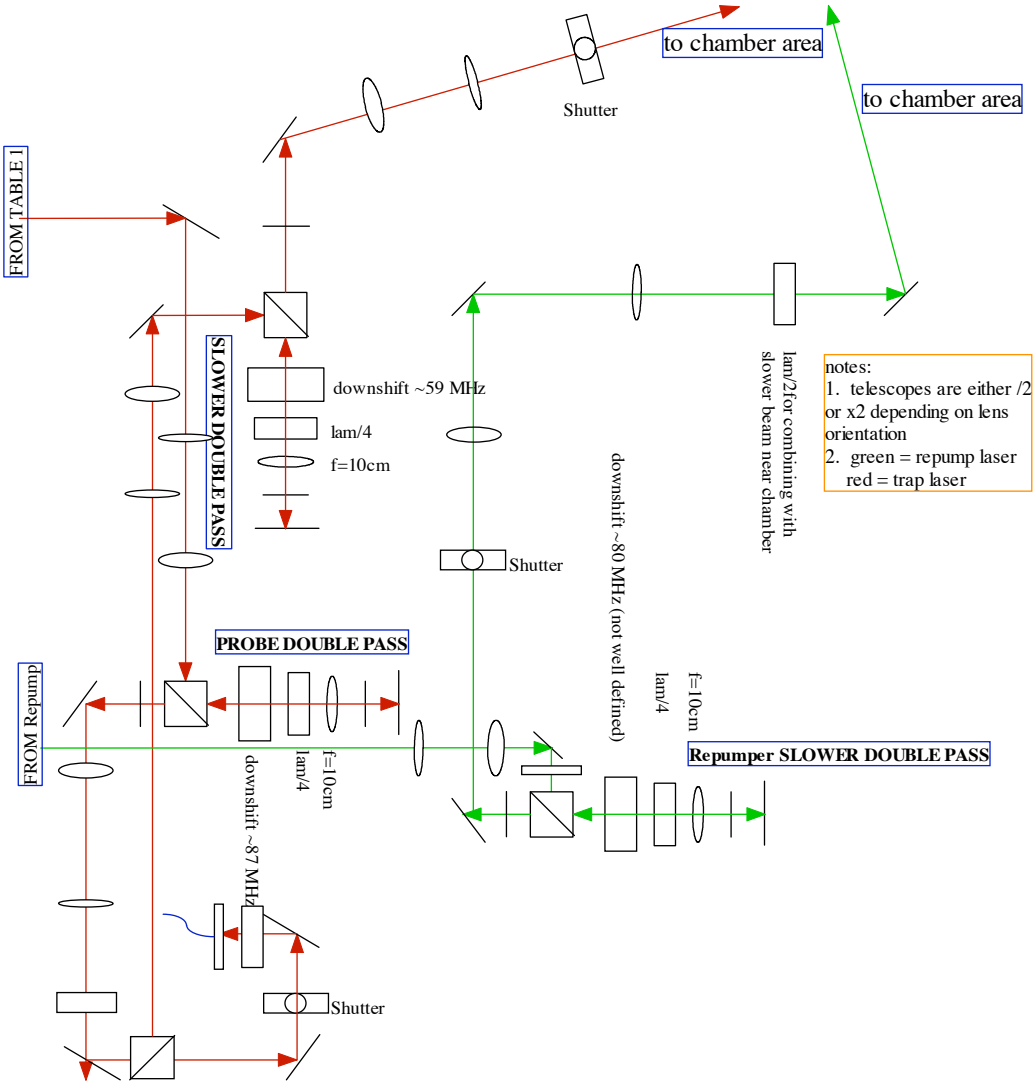

Figure 2.10: Diagram of layout on optical table for the Zeeman slower, Probe beam, and Slower repumper. Shutters are either Uniblitz or disassembled hard-drive.

2.5 Radio-frequency (rf) evaporation

The final stage of BEC formation is rf evaporation. As indicated in Fig. 2.12, a PulseBlaster card is encoded with a set of rf frequency steps. This sequence is programmed onto a frequency synthesizer (PTS-Ebay), then amplified (Mini-Circuits) and sent through an antenna (few loops of magnetic wire) situated externally on the bottom window of the main UHV-chamber. The antenna is elliptically shaped so as not to block the incoming MOT laser beams entering though the same window. The antenna is terminated into a 50 Ω attenuator.

The goal with rf evaporation is to remove the most energetic atoms that reside in the higher magnetic field regions of the trap. After the remaining atoms rethermalize through collisions, the cloud is colder. The rf field creates level crossings as a route for hot atoms to escape via spin flipping. As the rf is swept to lower frequencies, it accesses atoms further in from the edges of the trap. Because the rf field creates a dominant loss mechanism, when its frequency is below the depth of the trap determined by the B-field it defines the actual trap depth. During optimization of evaporation, one maximizes the increase in phase-space density (psd) over a given frequency ramp, which is given by $n\lambda_{dB}^3$, with the deBroglie wavelength, $\lambda_{dB} = \sqrt{2\pi\hbar^2/Mk_bT}$. n is the density, N/V. In a harmonic trap that does not change volume during the evaporation process, the change in phase space density (psd) is proportional to N/T^3. The efficiency of the process can be monitored using the parameter [36]

$$\gamma_{evap} = \frac{\ln(psd_{final}/psd_{init})}{\ln(N_{final}/N_{init})}. \tag{2.3}$$

The preferred optimization of the rf frequency ramp is as follows. Starting with a magnetically trapped sample that has been compressed to increase the density of atoms and thus the collision rate, one uses the rf knife to determine the "top" of the trap in frequency. Starting at that frequency, in our case 40 MHz, we pick a ramp step size and time, during which a measurable fraction of the atoms are lost, e.g. 40-30 MHz in 5 seconds. After this step, there is a hold time of 1 second at the final frequency, and then the atoms are released. The efficiency coefficient can be calculated or one can monitor optical depth (see Section 2.8). In this experiment, we find the atom cloud is not extremely sensitive to initial slopes of rf cuts. As the atoms cool, they become more sensitive to the ramp steps. As we add steps to the total ramp, previous steps are re-optimized. As a rule of thumb, the optical depth of the cloud should go up. Our magnetic trap lifetime was so short when the getters were used that the evaporation took 12 s and the BEC was small and short-lived. Currently, the lifetime is >50 s and we find that optimum evaporation times are 20-25 seconds depending on trapping frequencies. Weaker traps require longer evaporation times because of the slower rethermalization rate. A typical rf evaporation ramp (for a very tight trap and a decompressed trap) is shown in Fig. 2.11 with images of the cloud starting at 1 μK. The signature of BEC formation is the clear bimodal structure shown in the images (taken after expansion).

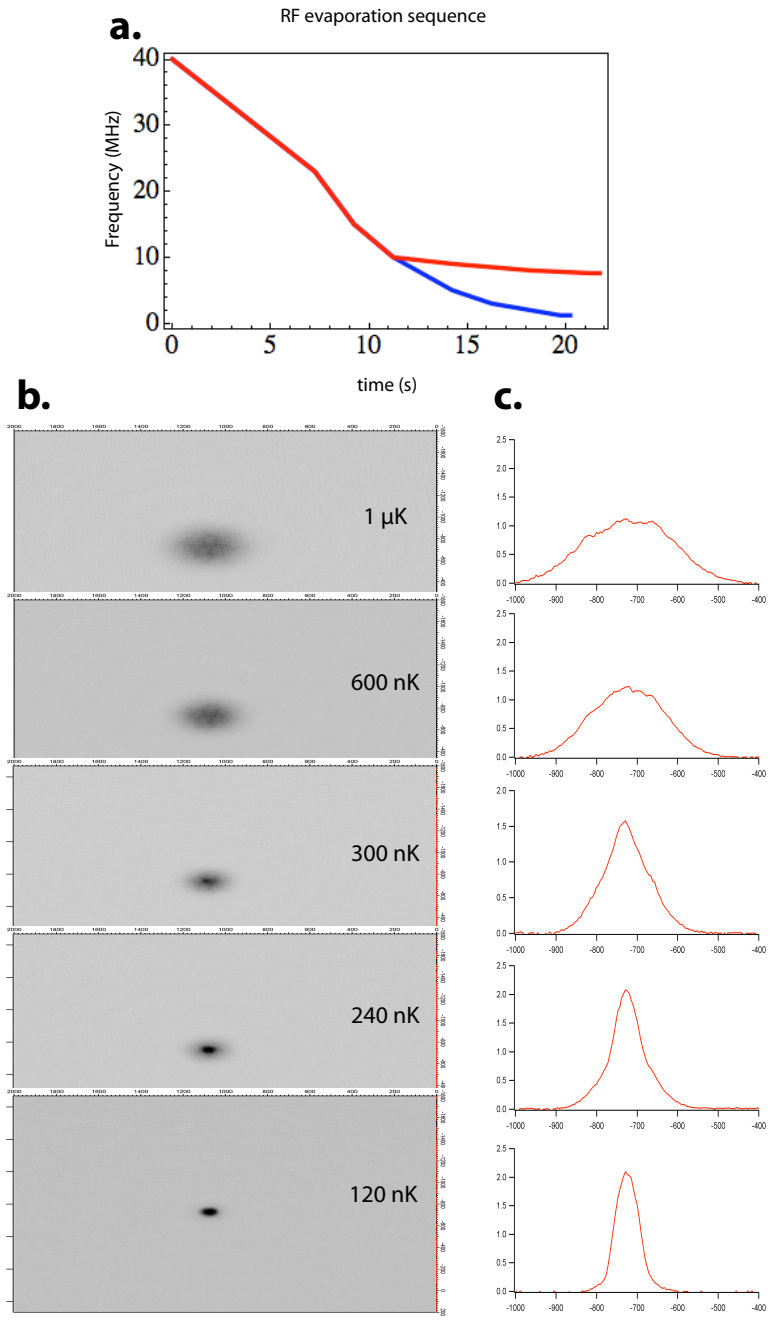

Figure 2.11: Fig. depicts (a.) typical evaporation sequence and (b.) absorption images of BEC formation. The red curve in (a.) is a ramp for a decompressed trap and the blue curve is the ramp in a compressed trap. The (b.) images and (c.) cross-sections were taken after the cloud was released from the magnetic trap and allowed to expand for 17 ms. The cross-sections in (c.) depict the clear bimodal distribution emerging as the condensate is formed. This corresponds to a high-density core shown in the absorption images in (b.).

2.6 Moving atoms: optical tweezer

After some evaporation, but prior to condensation, atoms can be moved to the glass science cell using an optical tweezer. The advantage of this design is the optical access to the atomic sample. Additionally, the proximity to the atoms allows for high resolution imaging (large numerical aperture, (N.A.)). Although I initially was involved in the design and use of this part of the apparatus, the experiments in this thesis do not use the tweezers. Thus, I will only introduce the technique here. The current lens design for our tweezer was determined and implemented by M. Beeler.

Alternative to a magnetic trap, a dipole trap provides all optical confinement for a neutral atom sample. An excellent review of this technique is Ref. [28]. Neutral atoms do not have permanent dipoles, but acquire an induced dipole moment from interaction with an oscillating electric field. This gives rise to an intensity-dependent force attracting atoms to the minimum or maximum of the potential depending on the sign of the detuning from resonance, Δ, the power, P, and the minimum waist, w_0. For alkali atoms, this potential, due to a focused Gaussian laser beam, is approximated as

$$U(r,z) \approx \frac{\pi c^2}{2}\left(\frac{2\Gamma_2}{\Delta_{2,F}\omega_{0,2}} + \frac{\Gamma_1}{\Delta_{1,F}\omega_{0,1}}\right)\frac{2P}{\pi w^2(z)} e^{-2\frac{r^2}{w^2(z)}} \tag{2.4}$$

Here, $w(z) = w_0\sqrt{1+(z/z_R)^2}$. z_R is the Raleigh range, $\pi w_0^2/\lambda$. $\Delta_{n,F}$ is the detuning of the laser from a ground state level, F, (in our case, 2) to either the $5^2P_{3/2}$ (n=2) or $5^2P_{1/2}$ (n=1) excited state. $\omega_{0,n}$ are the resonant frequencies of these same transitions. In this equation the counter-rotating term is neglected and I

assume linear polarization. For far-off resonant traps, the counter-rotating term contributes and is included in the calculation of trapping parameters. The scattering rate depends on detuning as $1/\Delta^2$ so the laser frequency must be tuned many linewidths away from resonance to attain long trapping times and low heating rates. Using $\omega_i = \sqrt{k_{s.c}/m}$ and $(\partial^2 U(0)/\partial i^2) = k_{s.c}$ (with i denoting direction x, y, or z and s.c referring to the spring constant), the trapping frequencies are calculated.

In our experiment in excess 10^6 atoms can be loaded from the magnetic trap into a beam of ∼1567 nm light focused to a minimum waist of 40 μm. The laser is a 15 W Erbium-doped single frequency, single polarization, fiber laser (IPG Photonics). The magnetic trapping stage is necessary because 1567 nm is resonant with a transition from the $5^2P_{3/2}$ state which prevents loading atoms from the MOT into the dipole trap. The small detuning from this transition gives rise to a large excited state light shift (hundreds of MHz using our powers). The level shifts closer to the ground state which makes the MOT cooling light look blue-detuned and therefore the atoms heat instead of cool.

The initial alignment of the dipole trap with the magnetic trap was difficult because of the small overlap region. A tracer beam could not be used for alignment because over the long pathlength 1550 nm mirrors transmit for 780 nm light (due to the anti-reflection coatings). Instead, we created a MOT cloud that was low density and spread over a large region. Due to the excited state light shift, the dipole beam slightly deformed this cloud. The Pixelfly camera (see Section 2.8), running in "live feed" mode can detect this deformation. From there we could load first cold atoms from a molasses and then walk the beam to the magnetic trap location near the

mirror surface.

The atoms, once transferred, are moved 25 cm to the glass cell by translating the waist slowly enough that the atoms follow (1.5 s, in our experiment). The focus lens is translated on an ultra-smooth air-bearing stage (Aerotech). This design was modeled after the MIT Ketterle group who first pioneered moving BECs. With our low density BECs, evaporation in a 1D dipole trap is too inefficient compared with the vacuum limited lifetime (15 seconds in the dipole trap) to be successful. Thus, when the atoms arrive in the cell, a secondary dipole trap intersects the cloud at a shallow angle to increase longitudinal confinement. We did not appreciate the low density problem in the initial design stages, and the experiment underwent many improvements before BEC was achieved in the science cell. For a more in-depth description of dipole trapping and its use in our current set-up, see the thesis of M. Beeler, in addition to the Refs. given here.

2.7 Optical lattices

The dipole trap section lays the theoretical foundation for the understanding of optical lattices. Lattices are a type of dipole trap using a standing wave, instead of a traveling wave [28]. The physics is the same; only the equations for the potential are slightly modified. The potential is

$$U(r,z) \approx U\frac{4P}{\pi w^2(z)}e^{-2\frac{r^2}{w^2(z)}}(1+\cos 2kz) \tag{2.5}$$

Here, U is the pre-factor which is dependent on detuning and atomic parameters [28]. The trapping frequency in the direction of propagation is approximately given

by $\omega_z = (2U(0,0)k^2/m)^{1/2}$ and is typically in the tens of kHz range. The atoms are attracted to the peaks or valleys of the standing wave depending on the sign of the detuning. The distance between each well of the standing wave is $\lambda/(2\sin\theta)$, where θ is the angle at which the two beams forming the standing wave intersect. This means that the condensate or thermal cloud is divided into pieces by the lattice. In a 1D lattice, this gives an array of 2D clouds of atoms shaped like pancakes (in deep lattices). All of the experiments described here use a 1D lattice. Experimentally, the lattice beams are not approximately collimated, but instead, are focused, which gives rise to additional dipole confinement. In principle one can design any arbitrary lattice topology to suit the user's needs. In the science cell, the optical access allows for such versatility. In order to add together optical lattices for this purpose, one just detunes the relative lattice beam frequencies by multiple MHz using an AOM. The high frequency interference term between two lattices is time-averaged to zero from the viewpoint of the atom sample.

All lattices in this experiment are derived from a tunable Ti-Sapphire laser peaked at 800 nm (Tekhnoscan). After frequency shifting with double-pass AOM set-ups, the individual beams pass through polarization maintaining fiber to clean up the spatial mode. Following the output couplers, the beams are directed into the chamber through the bottom window, where they are reflected off of the gold mirror. The lattices used are described in more detail in Chapter 3.

2.8 Imaging atomic clouds and time-of-flight

No matter the experimental sequence, we detect atomic samples using a technique called absorption imaging. If resonant light illuminates a sample of atoms, the amount of light remaining after absorption of photons in the cloud will depend on the density of the sample via

$$I(x,y) = I_0(x,y)\exp\left[-\sigma_{abs}\int n(x,y,z)dz\right] \tag{2.6}$$

Here, σ_{abs} is the absorption cross-section. The important quantity is the optical depth, O.D. (Eq. 2.7), which is extracted from this equation by taking two images: one with atoms and one without.

$$O.D. = -\ln\left(\frac{I(x,y)}{I_0(x,y)}\right) = \sigma_{abs}\int n(x,y,z)dz = \tilde{n}(x,y)\sigma l \tag{2.7}$$

We integrate over the z-direction (direction of imaging) to get a 2D density profile, $\tilde{n}(x,y)$. The imaging system currently in use was designed by M. Beeler. It has a magnification of $\approx$1. We acquire images of the sample in both the main chamber and the science cell. There is a 12-bit PixelFly QE (Cooke Corp.) camera for the main chamber (where the MOT/magnetic trap is formed) and a 10-bit Flea2 (Point Grey) for the glass cell (where atoms are moved to using the dipole trap), although in the future, the camera with higher dynamic range will be used in the chamber where most experiments take place. In the main chamber, the numerical aperture is limited by the radius of the vacuum chamber (9 cm). The imaging in the cell is limited by lens size, since we can get as close as 1 cm from the sample.

Absorption imaging does not work well when the sample is very optically

thick, as is the situation for a very cold cloud of atoms. The cloud will act like a lens and one will observe diffraction rings, distorting the image. For this reason, the atoms are first released from the trap and allowed to expand while falling (time-of-flight, TOF) prior to imaging. The resulting spatial distribution of the atoms is related to the momentum distribution. For a thermal cloud in a harmonic trap, regardless of the trapping frequencies, the cloud will be spherical after long TOF. In the long expansion time limit the initial cloud size is neglected and the temperature (measured along each direction of the cloud) is given by [38]

$$T_i = \frac{M}{k_B}\left[\frac{\sigma_i}{t_{TOF}}\right]^2. \tag{2.8}$$

Here, i denotes a direction and t_{TOF} is the expansion time. Typical expansion times range from 2 ms (for very hot or anisotropic clouds) to 25 ms (for BECs and atoms loaded into lattices).

For diagnostic purposes, there are additional cameras, which give a continuous live video feed to television monitors of the fluorescing atoms at the oven aperture and in the MOT region.

2.9 Computer Control and Data Acquisition

Shown in Fig. 2.12 is the flow diagram for computer control of the experiment. We use a PCI board called a PulseBlaster (SpinCore) to send digital signals to all equipment requiring a simple on/off during an experimental sequence. The PulseBlaster also triggers analog control boards to send specific voltages to types of equipment whose outputs are multi-valued during a sequence. Both the analog and

digital boards are programmed using code written in LabView and inherited from NIST (written by J.V. Porto and I.B. Spielman and modified for our experiment by M. Beeler). A secondary PulseBlaster card is used for the evaporation sequence described above in Section 2.5.

The camera takes an image with and without a cloud and the two are divided in a program in LabView and analyzed in IGOR (Wavemetrics). Most of the data acquisition software was also adapted from NIST by M. Beeler. For analyzing the multipeak results for the experiment described in Chapter 2, there are additional add-on procedure files, separate from the main analysis code.

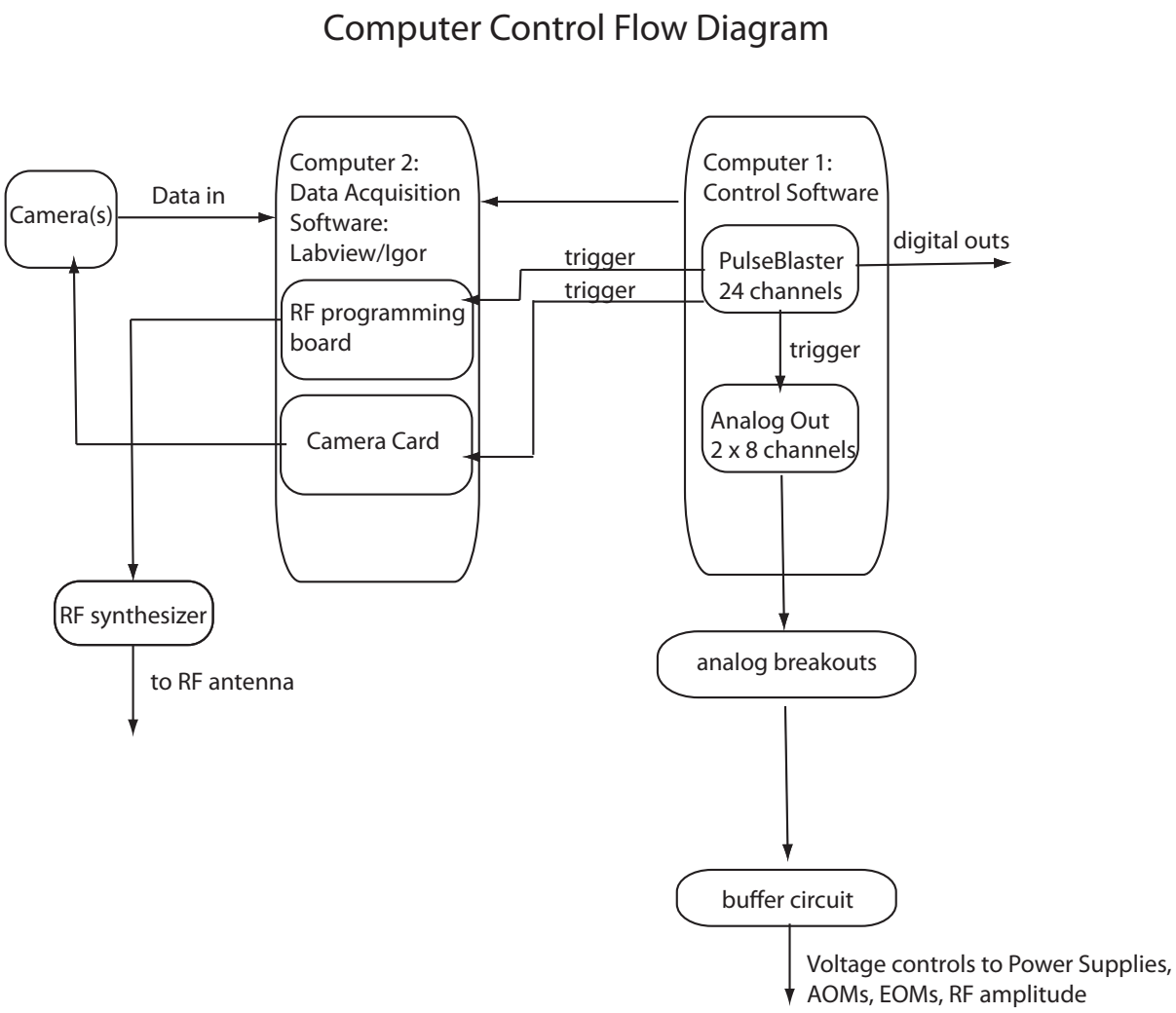

Figure 2.12: Flow diagram for the computer control and data acquisition of the experiment.

Chapter 3

Adiabaticity and Localization in Incommensurate lattices

3.1 Introduction and Motivation

Disorder plays an important role in many condensed matter systems,[22, 1] with deep connections to quantum chaos [27], but can be difficult to systematically study due to the challenge of creating reproducible and quantifiable disorder. Adding disorder to a lattice of bosons may give rise to a glassy phase (Bose glass) predicted between the insulating and superfluid phases. [22]. It is also responsible for exponentially localizing the wavefunction in a non-interacting system, so-called Anderson localization [1].

The control available in ultra-cold atom systems [8] has historically made them an attractive platform to study disorder [6, 53, 66, 61]. To date much of the work adding disorder to ultra-cold atom systems has explored time-independent properties, but the long timescales associated with cold atoms allows investigation of dynamical properties, as well (see [31, 58, 40, 6] and ref. therein). In these systems, atoms, which are $\sim 10^5\times$ more massive than electrons, have μs compared to ps dynamical time-scales. In this work we examine the ability of a quasi-disordered system to adiabatically follow changes in the Hamiltonian. The presence of disorder produces a complicated eigenvalue spectrum, which greatly affects the adiabaticity criteria. The physics of localization phenomena also has a significant impact on

time-dependent processes, such as adiabaticity. Small perturbations to the Hamiltonian can cause large changes to the ground state wavefunction over large length scales, making it difficult for the system to adiabatically follow changes. One recent theoretical study shows that adiabaticity in gapless systems is non-trivial, particularly in lower dimensions[49]. Here we show that even in a system where there is a well-defined separation between the ground and excited bands, such as is the case in our experiment, adiabaticity is complicated by the presence of disorder [21]. The following sections are an expanded description of the results which appeared in Ref. [21].

3.2 Disorder

From the condensed matter point-of-view there are different types of disorder, a few being dislocations, impurities, and random modulation of the energies, each producing different physical effects. In this work, we focus on random modulation of the periodic potential. Experimentally, the technique used to generate a random potential is to focus an optical speckle pattern onto the sample. In practice, producing a grain size small compared to the underlying lattice constant is difficult [41, 43], but can be accomplished by designing a chamber where a lens can be placed only 1-2 cm away from the sample (high numerical aperture) [66].

An alternative to approximating randomness is using incommensurate or two-color lattices [54, 13, 57, 55]. In an infinite, non-interacting system, the Aubry-André

Hamiltonian [3] describes the system:

$$H = J\sum_m (|w_m\rangle\langle w_{m+1}| + |w_{m+1}\rangle\langle w_m|) + \Delta\sum_m \cos(2\pi\beta m + \phi)|w_m\rangle\langle w_m|, \quad (3.1)$$

where J is the nearest neighbor tunneling and Δ is the amplitude of the disorder for an incommensurate lattice with the ratio of k-vectors, $\beta = k_2/k_1$. The localized Wannier states at site m are $|w_m\rangle$. This model predicts a crossover from a delocalized to an exponentially localized state for the ratio $\Delta/J \geq 2$ if the lattices are maximally incommensurate ([53, 27, 3] and Refs. therein). Presumably, deviations from the ideal incommensurate ratio, increases in interactions, and finite-size effects will change the predictions of this model [54, 57].

In this work, we study adiabaticity in a quasi-disordered system by adding one or two weak incommensurate lattices to a one-dimensional optical lattice loaded with a BEC. Localization occurs in both disordered and strictly incommensurate potentials [54, 57, 13, 61, 55], and it is assumed that differences tend to disappear in finite-sized systems such as ours. We observe a complex momentum distribution of the atoms due to the presence of weak perturbing lattices following a ramped loading process that would be nearly adiabatic for a single lattice. We gain insight into the distributions from single-particle band structure and observe that the effects of the perturbations disappear as interactions increase, as they suppress the long wavelength density modulation of the wavefunction.

3.3 Band Structure for Single Lattices

An excellent place to begin a description of atoms loaded into a lattice is single particle band structure [2]. The wavefunction of a particle in a given well of a periodic potential is related to the wavefunction in a neighboring well by Bloch's theorem,

$$\psi(r) = \exp(-iqr)\psi(r+R), \tag{3.2}$$

Here, R is a translation in the lattice and q is the quasimomentum. Quasimomentum is the phase of the wavefunction across adjoining sites in the lattice (it is equivalent to the term crystal momentum found in most solid state physics texts [2]). Because of the periodicity, the wavefunction and the potential can be rewritten as

$$\psi(r) = \exp[-iqr] \sum_m c_m^n \exp[-imGr] \tag{3.3}$$

$$V(r) = \sum_m V_m \exp[imGr], \tag{3.4}$$

where G is the reciprocal lattice vector defined as $2\pi/R$. The index m refers to the components of the momentum, n is the band index and V_m are the Fourier components of the potential. Using these substitutions, Schrödinger's equation becomes,

$$\left[\frac{\hbar^2}{2M}(q-mG)^2 + V_0\right] c_{q-mG} + V_G c_{q-(m+1)G} + V_{-G} c_{q-(m-1)G} = E c_{q-mG}. \tag{3.5}$$

From 3.5 the energy bands are calculated. The energy as a function of quasimomentum, q, is shown in Fig. 3.1 (presented in the reduced zone scheme) for the free particle case (top) and a lattice of depth 5 E_{rec} (bottom), where $E_{rec} = \hbar^2 k^2/2M$.

As shown in the free particle case (Fig. 3.1(a)), the ground and first excited state are separated by $4E_{rec}$. Stationary, non-interacting atoms have no means by

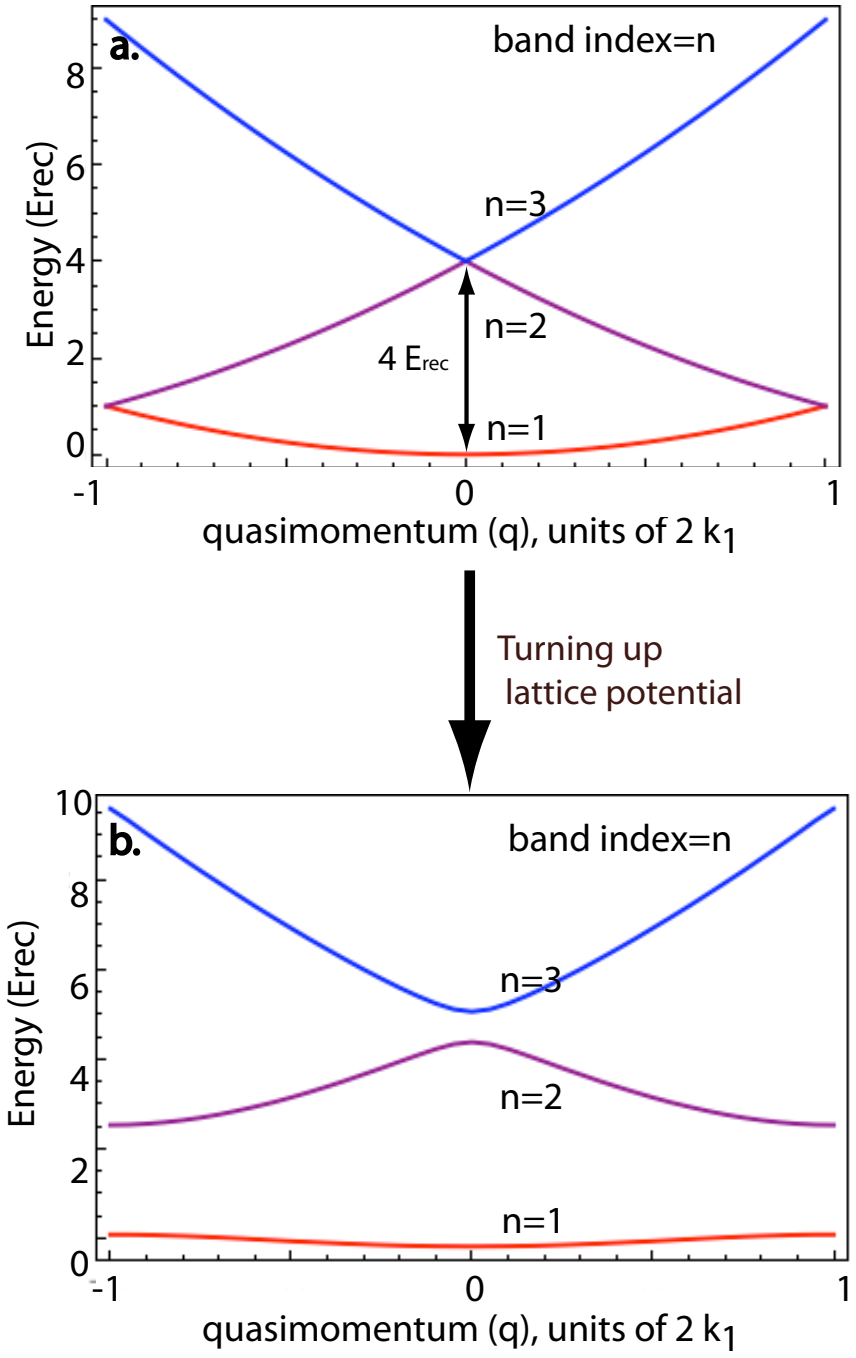

Figure 3.1: Energy bands as a function of quasimomentum for a free particle (top) and a single lattice potential (bottom). The bands are depicted in the reduced zone scheme. As the lattice is applied to the particle, the energy bands separate and the degeneracy at the edge of the Brillouin zone is lifted.

which to change q during the process of turning on or changing the amplitude of the periodic potential (when there are no other forces present). In our system, atom-atom interactions can change q, but the time scales are on the order of tens of milliseconds (see Section 3.4). This means that the relevant time scale for adiabatically loading atoms into the lowest energy band of the lattice is related to the separation between the ground and excited band.

The generalized time-dependent equation for calculating an excited state contribution is

$$\dot{a}_{n,q}(t) = \frac{a_{1,q}}{(E_{n,q} - E_{1,q})} \langle n, q | \frac{\partial H}{\partial t} | 1, q \rangle e^{i \int_0^t \frac{E_{n,q} - E_{1,q}}{\hbar} dt} \tag{3.6}$$

In order to remain adiabatic, the excited state population, $|a_{n,q}(t)|^2$, must stay $\ll 1$, where n is the band index other than $n = 1$ and q is the quasimomentum. One can calculate a corresponding time scale using Eq. 3.6 which, for loading a ^{87}Rb BEC into a single lattice at $k_1 \approx 2\pi/\lambda$, is satisfied for times much greater than 5 μs [59, 34, 47]. As the lattice depth increases, the bands continue to separate. Adiabaticity is most difficult for q near the band edge, where the initial energy gap vanishes. For our experiments, the initial momentum range is $\pm 0.15\ k_1$. Additionally, the single particle band picture begins to break down as the BEC becomes strongly interacting. The oft-cited adiabaticity expression [16, 59],

$$\left| \langle n, q | \frac{\partial H}{\partial t} | 1, q \rangle \right| << \frac{\Delta E^2(q, t)}{\hbar} \tag{3.7}$$

makes the approximation that the Hamiltonian and eigenstates are slowly varying and that the changes in energies are small. As we will see, these assumptions are not valid in the incommensurate lattice case.

3.4 Experimental details and results

As described in Chapter 2, we collect 10^9 atoms in our MOT. An optical molasses stage follows by abruptly turning off all magnetic fields and carefully zeroing the field at the atoms using the trim coils. During this phase, we reduce the intensity and detune the MOT beams a few linewidths further from resonance (to reduce the radiation pressure) using acousto-optic modulators (AOMs). This stage serves to cool the atoms to $\sim 40\mu$K. Because the atoms are so cold and do not move very much during this $\sim$5 ms stage, no additional forces are required to keep them in place. At this point the atoms are in an equal distribution of m_F levels, and we need them in a low-field seeking state, so we optically pump the atoms into the $|F = 2, m_F = 2\rangle$ state. We do this with a 100 μs pulse of circularly polarized light tuned to the $|F = 2\rangle$ to $|F' = 2\rangle$ transition. The polarization is given with respect to a quantization axis defined by a small field turned on in the B_y direction during the pulse. The magnetic trap is slowly ramped on and then immediately compressed to $\omega_x \approx \omega_z \approx 2\pi\times$410 Hz and $\omega_y \approx 2\pi\times$120 Hz to increase the density, and therefore the collision rate. We evaporatively cool the atoms until we obtain a condensate with less than 50 % thermal component (100 nK). To reduce the effects of interactions, which are density and scattering length dependent (Section 3.6), the trap is subsequently weakened giving final frequencies $\omega_x \approx 2\pi\times$40 Hz, $\omega_y \approx 2\pi\times$ 20 Hz, and $\omega_z \approx 2\pi\times$30 Hz.

3.4.1 Optical Lattices

We load the BEC into a 1D optical potential (recall Section 2.7, Optical Lattices), created by the addition of a primary and perturbing lattice(s). The lattices are created by reflection off an in-vacuum gold mirror (used for the mirror-MOT) situated approximately 2 mm from the magnetic trap center. As shown in Fig. 3.2, each beam is reflected at a different angle ($\theta_1 = 180°$, $\theta_2 = 143°$, and $\theta_3 = 155°$, defined as the angle between incoming and reflected beam) to yield a 1D pseudo-disordered potential [29]. The effective wavevector of each lattice is $k_{eff} = 2\pi/(2l)$ where the periodicity of the lattice, $l = \lambda/(2\sin(\theta))$. Because the gold mirror surface that defines the standing waves nodes is the same for all three lattices, they are phase-locked together, which gives a very stable potential. To prevent interference between the lattices, we detune the beams $\sim$160 MHz from each other with AOMs, so that the coupling terms between the beams oscillate rapidly compared to the atomic motion, and are time-averaged to zero (from the reference frame of the atoms). The $1/e^2$ waists for the primary perturbing beams are approximately 400 μm and 3500 μm, respectively. Fig. 3.2 depicts the lattice configuration.

The total potential is

$$V_{tot} = \frac{M}{2}(\omega_x^2 x^2 + \omega_y^2 y^2 + \omega_z^2 z^2) + V_1 \sin^2(k_1 z) + V_2 \sin^2(k_2 z) + V_3 \sin^2(k_3 z), \quad (3.8)$$

where M is the atomic mass, $k_1 = 2\pi/\lambda$, and $\lambda = 796.6$ nm. The ratios $k_2/k_1 = 0.806 \pm 0.002$ and $k_3/k_1 = 0.919 \pm 0.004$ are extracted from absorption images of atomic diffraction. The distance between momentum orders in each image, Δx, is extracted from an image. Using $\Delta x = vt$ and $p = Mv = 2n\hbar k$, where v is velocity,

t is expansion time, we calculate the k of the standing wave. The error bars reflect statistical uncertainty and include the error in position measurement. For the bulk of the experiments described here, the lattice depths are $V_1 = 4.6 \pm 0.3\ E_{rec}$ and $V_{2,3}/V_1 = 0.059 \pm 0.003$, where $E_{rec} = \hbar^2 k_1^2/2M$.

3.4.2 Lattice calibration

Although the potential is defined by clear parameters such as power, waist, and detuning, there is significant error in the power and waist measurements using standard equipment. The power can be measured with both a power meter having a silicon detector, which is sensitive at 800 nm. We measure the waist with a meter having a rotating silicon detector (Thorlabs) and also using a razor method. In the razor method, a blade is placed at the waist and its position is scanned horizontally through the beam in position steps much smaller than the beam diameter. The transmitted power is plotted as a function of position and fit to an error function curve. The waist is extracted from this curve fit. The errors arise from power measurement, position measurement with a micrometer, and placement of the razor blade.

The detuning is well known because we measure the wavelength on a wavemeter that is accurate to $\pm$ 30 MHz. For this reason, the individual lattice depths are calibrated using two alternative methods. In the first method, the laser is tuned close to resonance and a short pulse of light is imparted onto the sample. The effect of the pulse is to write a periodic phase on the wavefuction. The length of

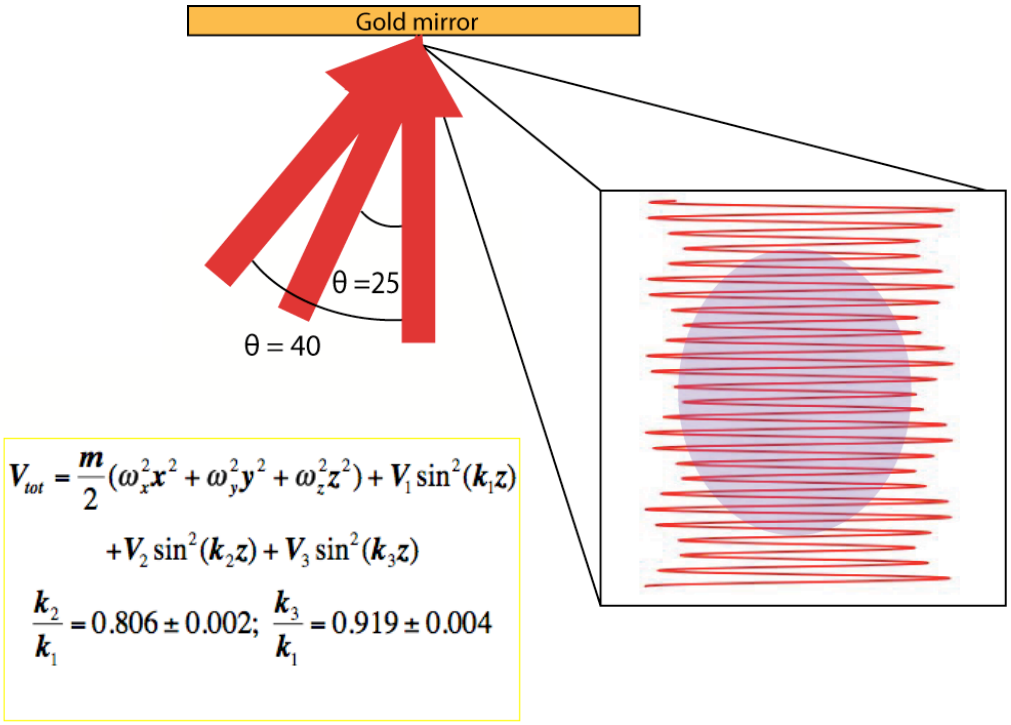

Figure 3.2: Beams propagating in the $+z$-direction are reflected off of an in-vacuum gold mirror forming a standing wave (in the gravity direction). They are reflected at different angles to give a 1D incommensurate lattice potential to mimic disorder. The depiction of the cloud in the lattice is not to scale. The approximate number of lattice sites occupied is $\sim$70.

the pulse, τ, is chosen to fall in the phase grating limit, where the atomic spatial wavefunction does not evolve in the wells of the standing wave. The condition for this is that $\tau << 2\pi/\omega_{latt}$. For a lattice with an estimated frequency of 20 kHz, τ must be much less than 50 μs. The resulting matter-wave diffraction pattern has momentum peaks spaced at $p_n = 2n\hbar k$, with n being an integer. The sample is cold enough (sub-1 μK) or condensed so that the expansion of the cloud in position is less than the expected spacing between momentum orders. The populations in the peaks are $P_n = J_n^2(\epsilon/2)$, where $J_n(z)$ are Bessel functions of the first kind [46]. The argument of the Bessel function is related to the amplitude of the standing wave by $\epsilon = \tau U(0)/\hbar$. $U(0)$ is the depth of the standing wave potential [28]. For good signal to noise, we choose a pulse which results in momentum components having equal amplitudes. The error from intensity fluctuations and power measurements does not contribute in this calibration measurement.

In the second calibration method, the atoms are loaded into a far-detuned lattice, and abruptly released. A gaussian fit is applied to each of the peaks in the resulting interference pattern. The relative populations in the ± 1 order momentum peaks (with respect to the 0^{th} order peak), $P_{\pm 1}$, are extracted and the depth of the lattice is determined from [11],

$$s = \frac{16}{[\ln(P_{\pm 1})]^2} P_{\pm 1}^{1/4} \tag{3.9}$$

We load the atoms into the combined lattices by ramping up the intensities, keeping a fixed ratio between $V_{2,3}$ and V_1. A ramp time of 1 ms is chosen for most experiments and is sufficiently long (compared to 5μs) to ensure loading a magnetically trapped

BEC into the lowest band of a single lattice (when no other lattices are present).

To assess our ability to adiabatically load a lattice, we perform two types of experiments. In all experiments, we take an absorption image of the cloud after 22 ms of expansion during time-of-flight. Following the ramped loading and a variable hold time (typically 1 ms), we turn off both the lattice and the magnetic trapping potentials. The image yields the momentum distribution of the atoms trapped in the lattice (interactions during time-of-flight are negligible).

3.4.3 Sudden release of atoms from a lattice and incommensurate potential

With a sudden release, the Bloch states are projected onto the free particle plane wave states with momentum, $p = \hbar q \pm 2n\hbar k$. For comparison, we present absorption images after the sudden turn-off, with and without the perturbative lattice(s) in Fig. 3.3. The existence of the weak perturbing lattice (Fig. 3.3(c-e)) markedly modifies the momentum distribution with the appearance of new peaks, even though the perturbing lattice is so weak that by itself it does not produce any diffraction with amplitude above our noise floor (Fig. 3.3(b)). In a system with perfect resolution, the momentum peaks would be observable. There is an enhancement of the peaks at $\pm 2\hbar k_2$ making them discernible above the image noise, as well as new features at $\pm 2\hbar |k_1 - k_2|$.

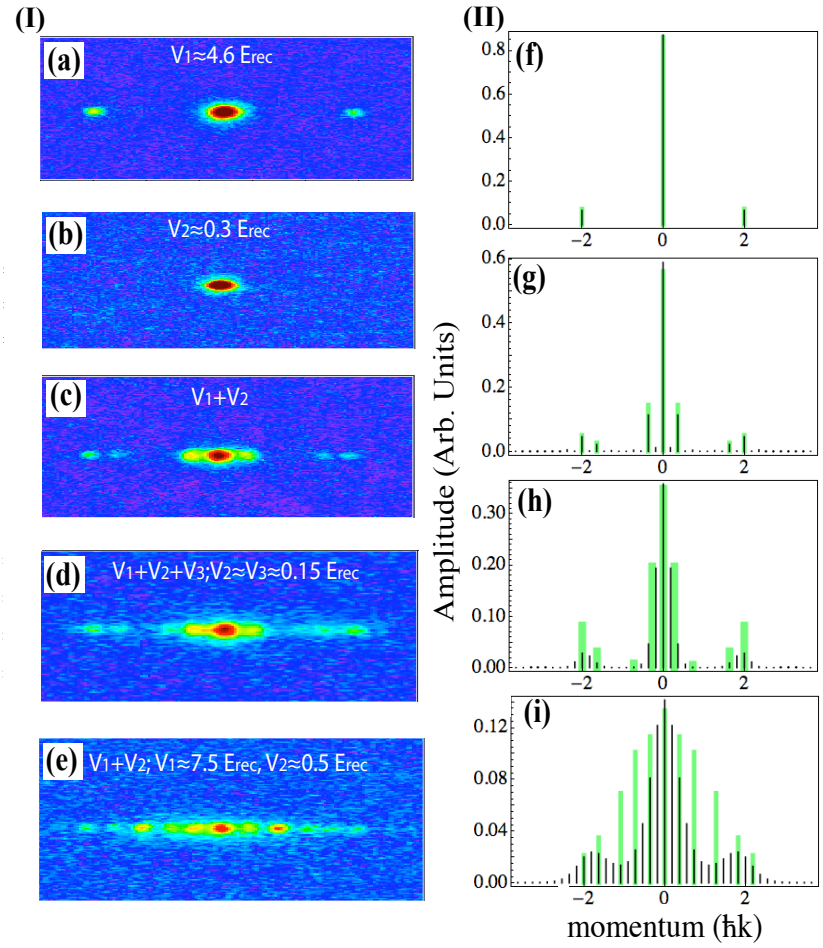

Figure 3.3: (I) Absorption images of a BEC loaded into different lattices for $\mu_{BEC} \approx 100$ Hz after 20 ms TOF: (a)$V_1 \approx 4.6\ E_{rec}$ and (b) $V_2 \approx 0.3\ E_{rec}$;(c) $V_1 + V_2$; (d) $V_1 + V_2 + V_3$, with $V_2 \approx V_3 \approx 0.15\ E_{rec}$; (e)$V_1 = 7.5\ E_{rec}$ and $V_2 = 0.5\ E_{rec}$ lattice. We turn on lattices using a 1 ms linear ramp followed by a 1 ms hold and abrupt turn-off. (II) Using the data from the absorption images ((I)-(a,c-e)) we extract the relative population amplitudes (green bars) and overlay them with a band structure calculation (no interactions) of the ground state momentum distribution (black lines).

3.4.4 Adiabatic turn-off

In the second method, after the loading and holding process, we slowly ramp down the lattice in 1-10 ms and then abruptly release from the magnetic trap (¡100 μs). If the process is fully adiabatic, the cloud should return to the momentum distribution of the original BEC. In Fig. 3.4, we present absorption images showing the results of testing for adiabaticity with a ramp-up/hold/ramp-down sequence. From Fig. 3.4a, one can see that the small perturbation prevents adiabaticity on millisecond time scales. After ramping down, there are momentum peaks separated by the difference in wavevectors, $k_1 - k_2$. One has to use perturbations less than $\sim$0.1 E_{rec} to prevent excitations during the experimental sequence (Fig. 3.4(c-d)).

It should be noted that as the perturbation has an increasing effect on the energy bands, it also becomes difficult to adiabatically turn-off the lattice.

3.5 Modeling results

We use single particle band structure and the 1D Gross-Pitaevskii equation to model our system.

3.5.1 Band structure to approximate incommensurate lattices

In order to understand why such a small perturbation has dramatic effects on the momentum structure and excited fraction we use single-particle band structure. Even if the perturbing lattice is strictly incommensurate with the primary lattice with $k_2/k_1 = \alpha$ equaling an irrational number, we can approximate α as a ratio of

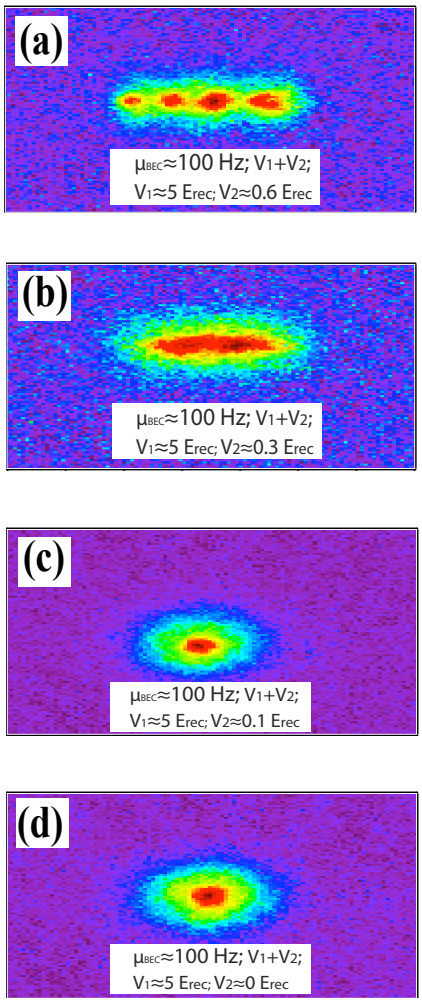

Figure 3.4: Results of adiabaticity check. (a)-(c) Absorption images following ramping off primary plus one perturbing lattice of differing strength. (d) Image of no lattices. These images illustrate the difficulty of adiabatic loading of a condensate into a pseudo-disordered lattice.

two large integers, f/g. In a finite system such as ours where the BEC occupies ≈ 70 sites of the primary lattice and does not extend over many periods of the beat frequency lattice (created by the combination of the lattice potentials) we expect this approach to yield reasonable predictions [17]. This modification gives rise to additional off-diagonal elements in the single period matrix (Eq. 3.5), which is then re-diagonallized to calculate the eigenvectors and eigenenergies.

Assuming no excitations to higher bands, we predict the momentum distribution for each lattice configuration using this modified band structure calculation with $f/g = 9/11$ and $f'/g = 10/11$, approximations to the experimental ratios. The integers in these ratios are not large (larger integers yield a more irrational number), but are chosen to give practical computation times. We increased the values to confirm that our calculations captured the features of the system. We present the results of this calculation overlaid with population amplitudes (green bars) extracted from fits of our data in Fig. 3.3. In the case of three lattices, experimental resolution limits our ability to resolve the structure, and this is represented by wider bars. The combination of the lattices creates a complex momentum structure, and the band structure calculation is in good qualitative agreement with our measurements. However, since the band-structure calculation assumes no excitations and a 1 ms ramp causes depletion of the ground band, the predicted populations do not quantitatively agree with the data for multiple lattices. This mismatch increases as the depths of both the primary and perturbing lattice(s) are increased. For deep lattices (Fig. 3.3(i)), depending on the choice of f/g , band structure predicts peaks spaced at k_1/g, closer than the beat frequency, yet the envelope does not change. We find

these disappear much more rapidly than the beat frequency peaks as interactions increase (see Section 3.6.1 below).

We also examine the changing wavefunction and the corresponding band-structure in Fig. 3.5. Using the $k-$vector of the primary lattice to determine the size of the first Brillouin zone, we plot the first two bands for the case of one and two lattices. The dominant effect of the perturbing lattice is to open small gaps in the ground band, as well as to slightly flatten the band between the new gaps. Starting at $q = 0$ and traveling along the band, the first gap corresponds to quasimomentum of $(k_1 - k_2)$. If instead one chooses the first Brillouin zone to span $\pm(k_1 - k_2)$ which is now much smaller, there exists a new band that is much lower in energy than the first excited band in the single lattice case, which determines a new energy scale relevant to adiabaticity. This new energy scale is also responsible for localizing the wavefunction at the spatial period corresponding to the beat frequency (Fig. 3.5(c) compared to Fig. 3.5(b)). The increased flatness of a band corresponds to a decrease in the tunneling rate because the energy states in the neighboring wells are no longer degenerate.

According to the new energy diagram, in order to satisfy the adiabaticity condition (Eq. 3.6, 3.7) for two lattices with our parameters ($V_2 \approx 0.059\, V_1, k_1/k_2 \approx 0.8$), the loading ramp must be much longer than 4 ms (a thousand times longer than for a single lattice). This is shown in Fig. 3.6(b), where we calculate the depletion of population in the ground band for different ramp rates as a function of primary lattice depth for the case of three lattices. From Eq. 3.5, modified for perturbing lattices when present, the coefficients, $c_{n,q}$, can be calculated for any

depth potential. If the change in the potential as a function of time is known, then the overlap of the eigenvectors can be used to calculate population as a function of ramp time. Starting with the free particle solution, the instantaneous eigenfunctions for a step in depth (time) are calculated and the overlap with the previous step is calculated. The result of this calculation is shown in Fig. 3.6(b). The inset of Fig. 3.6(b) depicts an expanded view of ramp times yielding less than 5 percent excitation.

Fig. 3.6(c) shows the depletion of the ground state as a function of lattice depth for a ramp time of approximately 2.5 ms for the case of one, two and three lattices. Since it is often the case experimentally that we start with a BEC with non-zero q (due to residual motion in the magnetic trap), we also show curves for loading a BEC with $q = 0.1\ k_1$ into a potential comprised of two and three lattices. This value of q was chosen to lie within the new, smaller first Brillouin zone and to fall within our experimental shot-to-shot fluctuations in q. These curves show that the effect of additional perturbing lattices is the dominant effect on adiabaticity criteria. For $q = 0.1\ k_1$, the adiabaticity time scale approaches 10 ms. We experimentally observe that by ramping up the potential and then ramping down with additional lattices, longer ramp times (5 ms compared to 250 μs) are qualitatively better (less excitations), but due to interactions, we are never able to be fully adiabatic. Although excitation to higher bands may also produce new momentum peaks, for the data presented in Fig. 3.3(c), we predict that between 1 and 5 percent of the population is excited depending on initial quasimomentum. Thus most of the observed changes in the momentum distribution can be ascribed to modification of the ground band

wavefunction, in this case localization.

The effects seen here are a result of the incommensurability of the lattices. For experiments using commensurate lattices [47] where two lattices had a carefully chosen ratio of 3:1, the criteria for adiabaticity with respect to the band structure is not significantly altered. In this case the higher order momentum peaks due to the perturbing lattice overlap the beat frequency peaks, which results in the wavefunction having modulation only at that spatial frequency. This difference can be seen by calculating the ground state wavefunction for the two cases. For approximately incommensurate lattices, the perturbation has a strong effect, with small spatial frequencies appearing (Fig. 3.5(c)). In order to further quantify this dramatic change, we plot the population of the $p = 0$ peak, p_0, as a function of lattice depth for a single lattice, and for a primary lattice with a perturbative lattice (with $V_2 = 0.059$ V_1, Fig. 3.6(a)). The black points are experimental measurements of the peak amplitude, which show a dramatic reduction of p_0 when the perturbing lattice is added. We show two band structure calculations for f/g=4/5 (dashed) and 9/11 (solid), both falling within the error bars of our experimental ratios. The significant difference between these cases is due to population growth in sub-beat frequency spaced momentum peaks predicted for the ratio 9/11. The error bars represent statistical uncertainties in populations and lattice depths (due to fluctuations in lattice beam intensity). We expect that because the turn-on of two lattices is not fully adiabatic there will be additional depletion of the central peak due to excitations into higher bands, as observed.

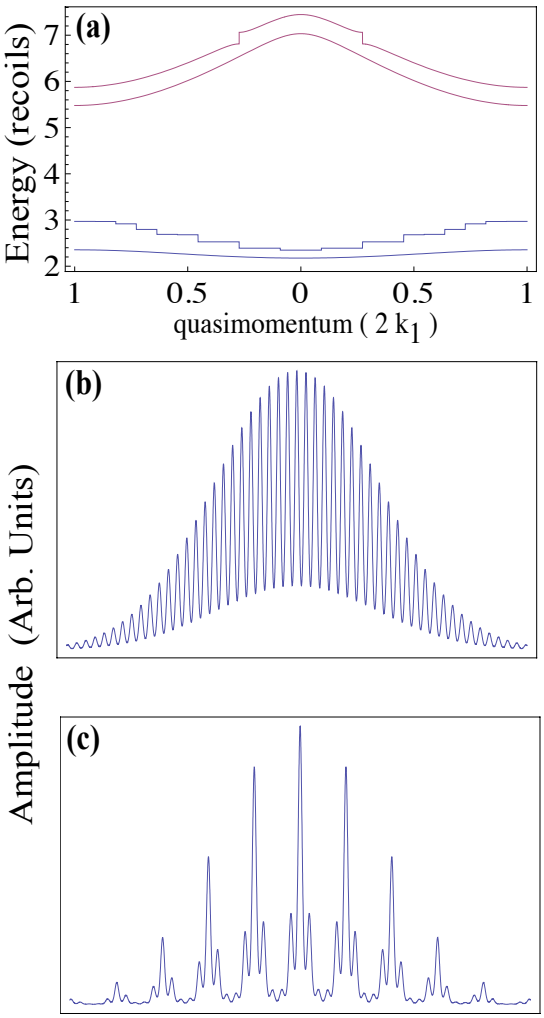

Figure 3.5: (a) Calculated first two bands for a single lattice and for two incommensurate lattices. Note the gaps which form in the ground band. (b-c) Plot of an example wavefunction multiplied by a Gaussian envelope (b) without and (c) with a perturbing lattice

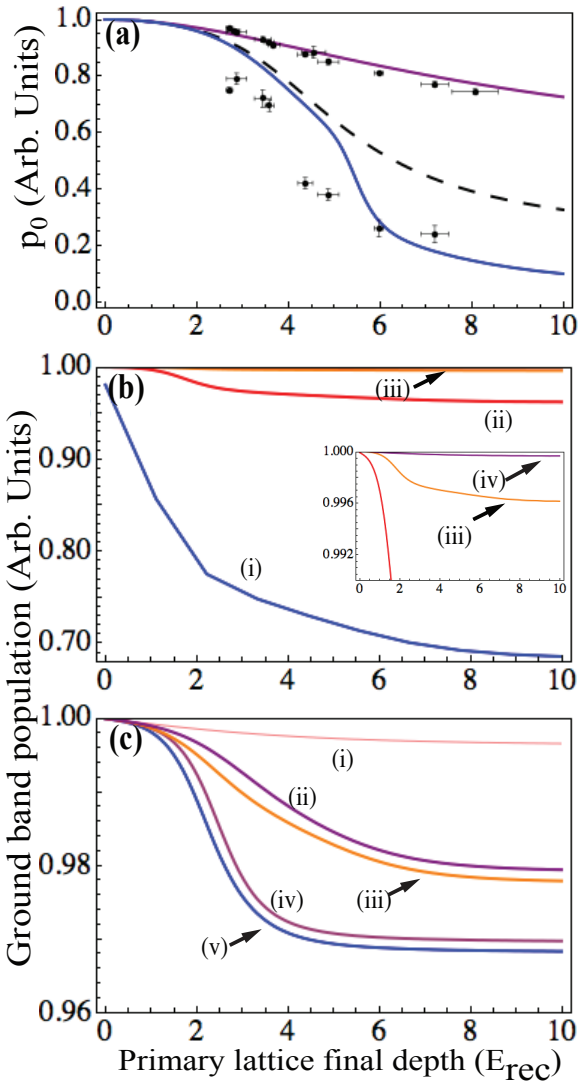

Figure 3.6: (a) the probability amplitude, p_0, as a function of lattice depth for $p = 0$ peak for the case of a single lattice (V_1) and a combined potential ($V_2 \approx 0.06V_1$). The changes in slope correspond to the depths at which the atoms become localized at different spatial frequencies. (b) Calculation of ground band population for differing ramp times for case of three lattices ((i) 25 μs, (ii) 250 μs, (iii) 2.5 ms). The total perturbation is $V_2 + V_3 \approx 0.06V_1$; (iv) Result of loading a single lattice with a ramp time of 2.5 ms. Inset in (b) is a zoomed-in view for comparison of (iii) and (iv). (c) Calculated ground state population for loading a (i) single lattice, (ii) two lattices, (iii) two lattices starting with $q = 0.1$ and three lattices starting with (iv) $q = 0$ and (v) $q = 0.1$ for a fixed ramp time of 2.5 ms.

3.6 Localization

There are many types of phenomena classified as localization. In the context of the experiments described here, the term localization refers to decreasing the spatial extent of the wavefunction. In the limit of a non-interacting, infinite system in the presence of a disordered potential, Anderson predicted [1] that the wavefunction would become exponentially localized through destructive interference of wave reflections. In 1D systems, the wavefunction is always localized for a finite amount of disorder, whereas in higher dimensions a transition from extended to localized states is predicted. In practice cold atom experiments are finite systems and without a Feshbach resonance to tune the scattering length, a, to zero (see for example [53] and Refs. therein), these systems also have non-negligible interactions.

In this experiment the disorder is formed by an incommensurate lattice and localization associated with this Hamiltonian is predicted using the Aubry-Andre model [56, 53, 55]. Compared with Anderson-type localization, this model predicts a transition from delocalized to localization even in 1D systems. In both the Anderson and Aubry-André model interactions still compete and are predicted to destroy the localization effects (recall Section 3.2).

In our weakly interacting system, we see the production of low spatial frequency, long-wavelength components in the wavefunction with the application of weak incommensurate lattices. This yields insight into the connection between disorder, localization, and incommensurate systems. In the canonical view of localization, destructive interference due to reflections over long distances leads to the

localization of the wavefunction[1, 56]. Here we see that a single incommensurate perturber yields a complex long wavelength structure. If we add a second perturber, getting closer to true disorder, we see even more momentum components and calculations show the amplitude of the wavefunction is suppressed. Experimentally, due to finite resolution, this appears as a broadening of the distribution (Fig. 3.3(d)). Comparing three lattices to two, we observe a larger spread in the central feature, as well as a corresponding decrease in optical depth. This indicates that there are unresolved peaks beneath the overall envelope. In Ref.[54] it was suggested that an indication of localization is the appearance of additional momentum peaks in the matter-wave interference pattern. If something competes with these long range interferences, such as atom-atom interactions, we can expect localization phenomena to be drastically modified [40]. Indeed, until recently [53, 6] Anderson localization had not been seen in cold atom systems due to the effect of atom-atom interactions.

3.6.1 Adding interactions: 1D Gross-Pitaevski equation

To study the effects of interactions in our system, we perform experiments in three different magnetic traps of differing frequencies with chemical potentials of $\mu_{BEC}/h \approx (2500, 400, 100)$ Hz. μ_{BEC} is calculated from

$$\mu_{BEC} = \frac{1}{2\hbar\omega_{ho}}\left(\frac{15(1-T/T_c)^3 Na}{a_{ho}}\right)^{2/5} \tag{3.10}$$

Here, ω_{ho} is the geometric mean of the harmonic oscillator frequencies, $2\pi(f_x f_y f_z)^{1/3}$, a_{ho} is the harmonic oscillator length equal to $\sqrt{\hbar/(M\omega_{ho})}$. We observe (Fig. 3.7)

that as the overall confinement is increased, both the structure in the interference pattern such as the $k_1 - k_2$ momentum peaks disappears and the overall size of the cloud, after TOF, increases.

We compare the results of the non-interacting band-structure model to simulations of our system using the Gross-Pitaevskii equation (GPE),

$$-\frac{\hbar^2}{2M}\nabla^2\psi(r) + V(r)\psi(r) + g|\psi(r)|^2\psi(r) = \mu\psi(r). \tag{3.11}$$

This is Schrödinger's equation with a non-linear term with the coefficient, $g = 4\pi\hbar^2 a/M$. Here, a is the s-wave scattering length. This equation assumes that the mean field approximation is valid where the wavefunction is a product of single particle indistinguishable wavefunctions. It is most accurate when the system modeled has only small deviations from BEC. In our system, this assumption may not be true because of the localizing effects at weak interactions; however, the results of the calculation match well with our observations. For more details on the GPE and approximations for condensates, see Ref. [48, 12].

We reduce the 3D equation to 1D and solve using the split-operator method in combination with imaginary time evolution [4]. Although our system is not 1D, but an array of 2D pancakes, this reduction method captures the main features of our results. The simulations using the GPE predict that in the moderately tight trap ($\mu_{BEC}/h = 400$ Hz), the $k_1 - k_2$ (beat frequency) peaks slightly persist, however they disappear in the tightest trap. Fig. 3.7 shows absorption images with results of GP simulation in three different traps. In our system, we cannot decouple the size of the sample from interactions (since we increase interactions by compressing

the trap which decreases the size), which both contribute to the amount of spatial localization. This can be done if one utilizes a Feshbach resonance, as in [53], to vary the strength of the scattering length, a.

We calculate the effect of arbitrarily increasing the interactions in our weakest trap (where the structure is most apparent) and see that the sub-beat frequency peaks vanish rapidly, followed by the $k_1 - k_2$ peaks. This can be understood in that interactions drive transitions between states of different quasimomentum, washing out the discrete low momentum features, and destroying the long range spatial periodicity of the wavefunction. The GP simulation also includes the harmonic potential that is neglected in the band structure calculations. Simulations with our experimental parameters show that in the limit that interactions do not dominate (lattice depths $< 7\ E_{rec}$), the harmonic trap increases the effects the secondary lattice has on the adiabaticity condition. For additional results of GPE calculations, see thesis of M. Beeler.

3.7 Conclusions

In conclusion, we have presented data indicating that small perturbations to a one-dimensional lattice system in the form of quasi-disorder, while leading to localization of the wavefunction, also drastically change the dynamics of the system. We present a theoretical treatment which suggests that although we are only slightly modifying the energy of the system, the large alterations of the wavefunction demand time scales for adiabaticity that are orders of magnitude longer than for loading a

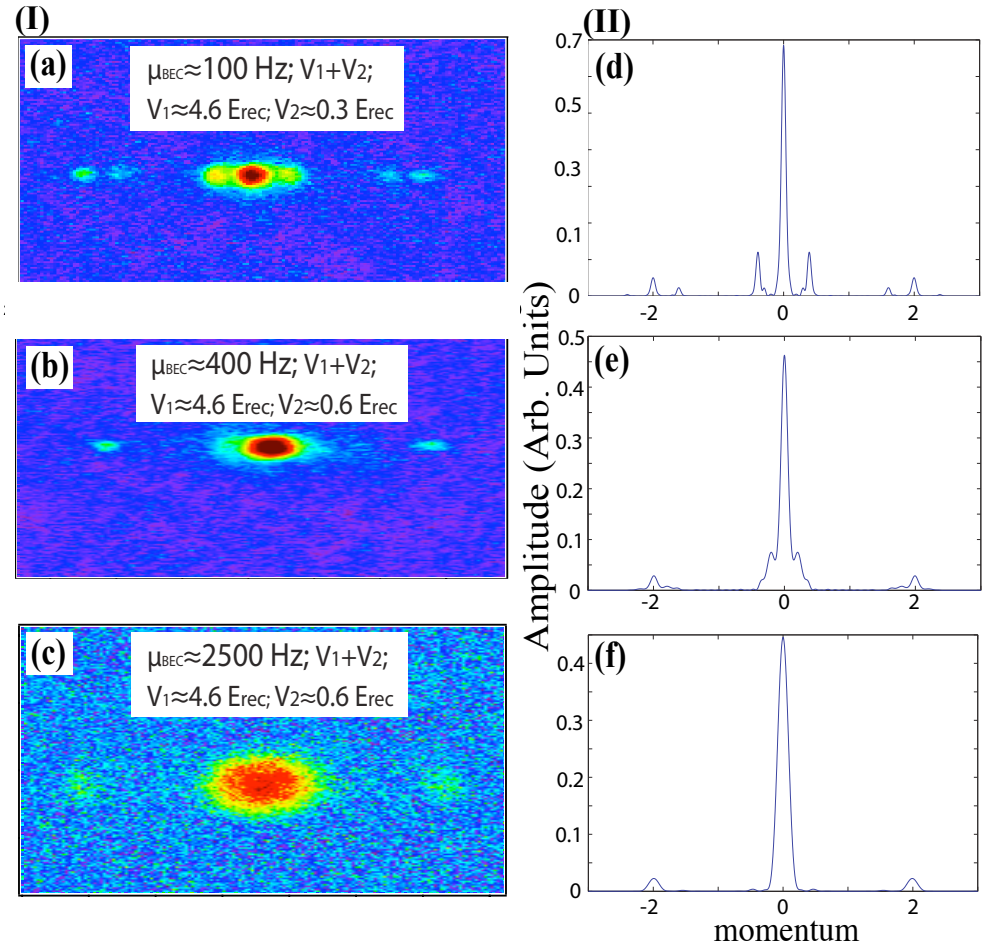

Figure 3.7: (I) (a-c) Absorption images in traps with $\mu_{BEC} \approx (100, 400, 2500)$ Hz with primary lattice plus one perturbing lattice. (II) (d-f) Results of GP simulation for (a-c) qualitatively showing the effects of interactions.

single lattice. Because of the sensitivity of the adiabaticity criteria in the presence of perturbations, one should be careful when studying disordered lattice systems to identify and characterize any forms of disorder present in the potential, intentional or otherwise. This work shows that disorder can have a strong influence on dynamics, and that the long timescales of cold-atom optical lattice systems makes them ideal for further explorations.

3.8 Comments and Future directions

3.8.1 Incommensurate lattices as a model for disorder and finite-size effects

In our type of system, two important questions are (1) how well does the system approximates true disorder and (2) how much does the finite-size of the system matter. These are subtle questions, which remain open for further study.

Incommensurate lattices are defined as having a ratio of k-vectors that is an irrational number. Two lattices that have a ratio that approaches the golden mean are said to be maximally incommensurate (see [53, 55] and Refs. therein). In a finite-size system, the effects of deviating away from the incommensurate lattice's ratio are not known. Intuitively, it seems that if the atomic cloud only extends over a small length of the lattice, the potential it feels is pseudorandom and only in the limit of infinitely long condensates do differences appear. This would be interesting to be able to study, if one could arbitrarily control the k-vector ratio over a variety of irrational numbers and characterize the irrationality of the ratio with respect to

the golden-mean.

An experiment such as this would also be able to investigate how closely a finite-sized incommensurate system mimics random disorder, i.e. a potential formed from speckle. We expect that adding an infinite number of incommensurate perturbers would perfectly mimic true disorder. Experimentally, this is not feasible, but in a finite size system, we expect that many fewer perturbers would be necessary to accomplish this. Although in [66], they are in the strongly interacting regime, it is clear when comparing momentum distributions from their experiment and others using speckle with our results [21] and those found in Ref. [53] that there is a fundamental difference between the two types of randomness. It would be very interesting to investigate the length scales over which this is experimentally valid.

3.8.2 Excited state populations

Using the adiabaticity condition, one can predict the growth of population into higher bands of the lattice. This calculation is shown in Fig. 3.8. From the calculation, it is predicted that the population of excited bands grows and different bands dominate for different depths.

We previously attempted to characterize the excitations (with stronger perturbations) by letting the excited fraction relax into the thermal component. After loading the BEC into the lattice(s) and holding for 1 ms, we ramp off the intensity of the lattice(s) in 1-20 ms. The sample is held in the magnetic trap for a varying amount of time. During this hold, we assume that the excited fraction (due to non-

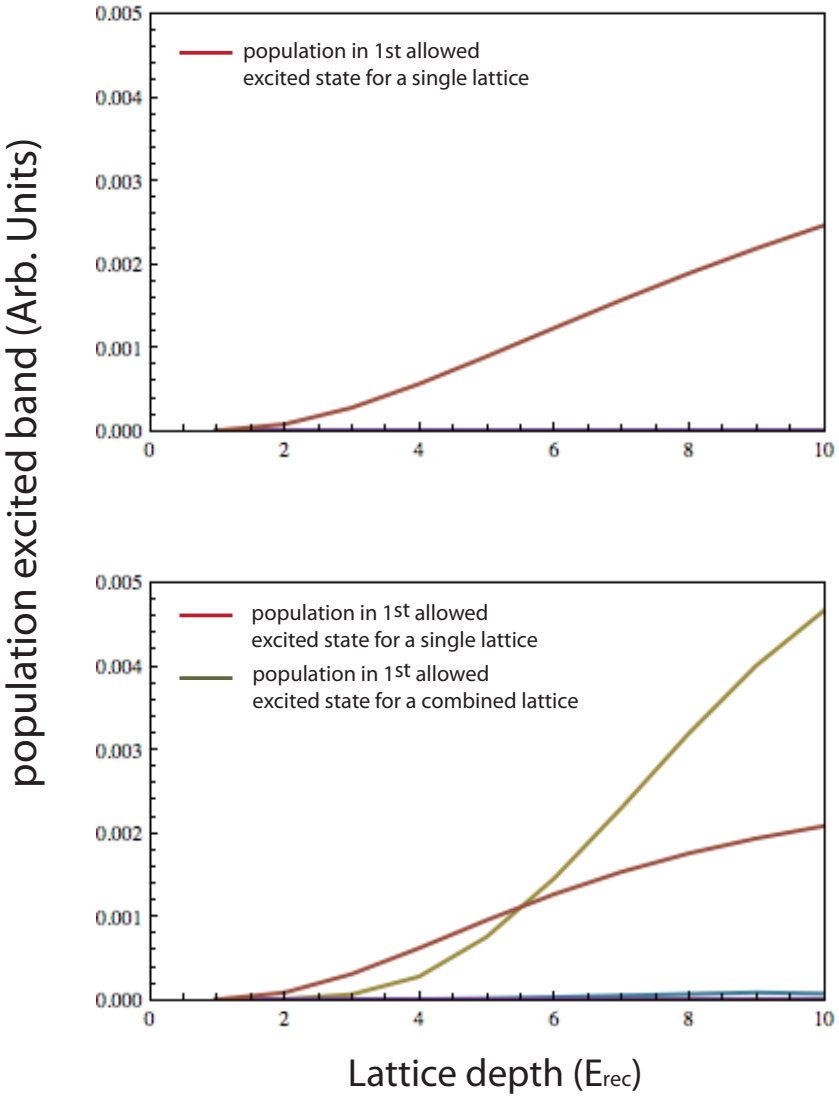

Figure 3.8: Comparing excited band populations for one and two total lattices. The strength of the perturbation is 6 percent of the depth of the primary lattice. After the strength of the primary lattice reaches a critical value, population growth accelerates in the band which corresponds to the 1st excited state of the approximate $k_1 - k_2$ lattice.

adiabatic loading) will relax into the thermal component in the magnetic trap. We do observe qualitatively that for very short loading times (compared to the band separation) a large thermal fraction emerges. However, this was difficult to quantify because the lattice turn-off induced breathing modes which did not damp on experimental time-scales. Additionally, if the turn-off of the lattices induces additional excitations, the two effects cannot be decoupled.

3.8.3 Band-mapping

Currently, we are working on a third, more comprehensive, experimental test for adiabaticity. We will use a well-known technique called band-mapping in an attempt to quantify excited state populations. After loading the atoms using the same sequence as above, the lattice is turned off fast compared to many body interactions, but slow compared to single particle excitations. The populations from each band are mapped onto the Brillouin zones (ground band populations in first Brillouin zone, first excited band populations map to second Brillouin zone, etc). This is a tricky experiment, because as we have shown, the perturbing lattice drastically modifies the energetics of the system. We anticipate that this technique will break down as the band gaps close. We will start with a primary lattice and slowly increase the perturbation to characterize this behavior.

Chapter 4

Final remarks

The study of BECs in disordered potentials is a rich field of study and there are several experiments for which this apparatus is well-suited. I have described the first results from this apparatus and this section will briefly describe a few future experiments that I have had a role in planning.

4.1 Non-equilibrium dynamics and the effect of lattices on the formation of BECs

Classical and quantum systems typically achieve equilibrium through exchange of energy with the surroundings. For example, in a system of a dilute, thermal gas of neutral atoms confined to a harmonic trap undergoing cooling to Bose-Einstein condensation (BEC), these exchanges are in the form of collisions with atoms that can subsequently leave the gas. In a crystal, there are exchanges of energy through phonons and the atoms are "pinned" to sites through chemical interactions. The BEC-optical lattice is the atom-optic version of the solid-state crystal, but there are no phonons and typically no evaporation so the system is isolated from the environment. In an interacting system, particle-particle interactions play a role in distributing energy among particles, even if the system is isolated from a reservoir.

Previous theoretical models of non-equilibrium dynamics have focused on de-

veloping a quantum picture of the Kibble-Zurek mechanism (KZM) [37, 68]. The standard picture of this mechanism is that far away from a phase transition, the system dynamics are adiabatic because the relaxation time, τ, is short, but as one approaches a critical point, τ diverges. If one quenches the system, defined as crossing the transition in a time, t_Q, faster than τ, the system is driven out of equilibrium. Thus, after the transition is passed, the order parameter will develop domains of differing phase giving rise to topological defects such as vortices. Because this critical slowing down of the relaxation is inherent in the phase transition, the formation of defects is inevitable; however, their persistence and density is dependent on the speed of the quenching. This mechanism was initially developed in a classical system with applications to defect formation in the early universe [37]. It has been shown that features of the KZM can be mapped onto systems exhibiting quantum phase transitions (QPT) such as the MI-SF transition [30, 20].

Quenching across a phase boundary has been used recently to observe vortices during the BEC transition in an ultra-cold atom system [64]. We have begun studying the dynamics of the condensate transition in the presence of a perturbing potential. We evaporate to just above T_c and subsequently turn on a 1D lattice potential created in the manner described in Chapter 3. We continue the evaporation process and observe the establishment of phase coherence between lattice sites. The lattice potential is expected to slow down the re-thermalization process by affecting the collision rate. Indeed, we have observed that evaporation in the presence of a weak lattice ($\approx 5\ E_{rec}$) dramatically slows the equilibration process. The goal is to measure this re-thermalization process and the dynamics that lead to relaxation

when the system is quenched into a regime that would be condensed. This class of experiments investigating the KZM are interesting in terms of the defects and give insight into resulting effects of a quench. The initial and final states of the system are near-equilibrium, but the system is driven out of equilibrium near the phase boundary.

Our system design, with the mirror defining the nodes of the lattice potential being $\sim$2 mm from the atomic sample, is ideal for the long time-scales for this study. Recent observations suggest that the time for relaxation is on the order of seconds, which translates into needing low loss and small heating rates. The versatility of our system provides a platform for extending this study of non-equilibrium phenomena in a single period lattice to the effects of disorder. Because we can load the atoms into an incommensurate lattice and plan on implementing a speckle potential we can span the range from quasi-periodic disorder to true disorder. As previous experiments have shown, the signatures of disordered phases such as glasses can be difficult to interpret. A potential method for further identifying a glassy phase may be the observation of diverging equilibration time-scales through these non-equilibrium experiments.

4.2 Bloch Oscillations

As described in Section 3.2, when a BEC is trapped in an optical lattice, energy bands arise due to the periodicity in the system. In a perfect lattice without defects, the application of a constant force, such as that due to gravity, causes the

atoms to oscillate in position and momentum, undergoing Bloch oscillations. The period of oscillation is $T_B = 2\pi\hbar/Fd$. Here, F is force and d is the lattice constant. In our system, the lattice(s) are oriented in the direction of gravity, so we utilize this as our force. Adding a perturbation to the lattice in the form of disorder, or pseudodisorder (incommensurate lattice) will damp these oscillations. The disorder breaks the symmetry and the energy levels become unequally spaced. This induces dephasing of the matter-wave, thus damping the oscillations [60]. In solids, disorder completely destroys Bloch oscillations which results in a finite resistance.

If instead, one makes the force time-dependent with an oscillatory frequency of $1/T_B$, one can observe coherent delocalization of the condensate [32]. In the presence of both the disorder and the time-dependent force, there is a competition between these two localizing effects [31]. We are studying this in our BEC-1D lattice system. Thus far, we have observed that minimal disorder will lead to strong damping of the Bloch oscillations.

4.3 Delta-kicked harmonic oscillator

Previous to experiments with disorder, we unsuccessfully tried to observe resonant features in a quantum δ-kicked harmonic oscillator. We hope to revisit this project because we have made improvements to increase the stability of the system, which may allow us to observe resonances.

The goal of this experiment was to study the delta-kicked harmonic oscillator in the context of a quantum mechanical system. Classically there are systems

exhibiting chaotic phenomena, such as the δ-kicked rotor. In order to better understand the meaning of quantum chaos, one can choose the quantum analog of these classical systems and observe their behavior. The delta-kicked rotor has been studied in the context of cold atoms previously [44]. If one calculates the effect of adding in a harmonic term, as exists for a magnetic trap, then under certain conditions there are resonances (where the energy increases dramatically). The Hamiltonian for this system, ignoring interactions due to a possible condensate fraction, is

$$H = \frac{p^2}{2m} + \frac{M\omega_z^2 z^2}{2} + V_0 \tau_p \cos^2(k_{latt} z) \sum_{n=0}^{\infty} \delta(t - nT_K) \tag{4.1}$$

Here, V_0 is the strength of the pulsed standing wave having k-vector, k, and pulse width, τ_p. n is the number of times the sample is kicked in a harmonic potential with a trapping frequency, ω_z.

The δ-kicked harmonic oscillator is also interesting because applications to electronic transport and it exhibits a "crystalline" phase space [35]. The effects of non-linearity on this system due to the presence of a condensate has been investigated theoretically [25] and to our knowledge, only one experiment has attempted to study this system [19]. We performed calculations on our system to determine the parameters for the resonances. We designed an experiment loading a cold cloud ($\sim 0.5 - 1\mu$K) into an approximately cylindrically symmetric harmonic trap formed by magnetic fields (see Chapter 2). We chose a non-condensed cloud because the non-linear term does not contribute. We applied short kicks in the form of standing waves to the atoms and monitored the energy as a function of kick number and kick strength. These kicks were in the regime of a phase grating (Section 3.3.2).

While the δ-kicked rotor is a relatively simple experiment, the δ-kicked harmonic oscillator, although seemingly a small extension, is much more sensitive to experimental details. It requires exquisite stability in the harmonic trapping frequencies. If these frequencies are changing during the kicking sequence, the resonances are predicted to broaden, or even disappear. Instabilities due to current variations in the power supplies can cause large fluctuations in the magnetic fields. Analysis showed that variations in the relative positions of the trap center and standing wave washed out the resonances. We were not able to remove all the noise from the system and thus did not observe resonances.

Appendix A

Inventory

The following is a list of the major components of our apparatus.

A.1 Vacuum

Part Number **Vendor**	**Part Description**
MCF600-SO200800-A Kimball Physics	Spherical Octagon vacuum chamber
9191145 Varian Inc.	Varian starcell diode ion pump
9290191 Varian Inc	Mini-vac ion pump controller and cable
274042 Granville-Phillips	Dual filament nude bayard type ion gauge
350501-A-T1 Granville-Phillips	Ion gauge controller-350 and cable
Custom Kurt Lesker Inc.	Custom feed-throughs
SG0150MCCF Kurt Lesker Inc.	Manual gate valve
B1381S Bomco	Glass to metal seal 2.75 inch con-flat flange
Rb/NF/6.4/17/FT (website) SAES getters	Rb-Alkali metal dispensers
37-3736	Argon packed Rb glass ampoule, 1g

Strem Chemical	
MCF450-SS20400-A Kimball Physics Inc.	Spherical Square vacuum chamber
VA-30-DD-M, V-410-MS Duniway stockroom	Varian-type 30 L/s ion pump and cable
IPC-0062 Duniway stockroom	Ion pump controller, diode or triode
for custom flange Kurt Lesker	rotary feedthrough piece (source)
custom Stratamet, Inc.	AlN mount for wire traps
custom Spectrum ThinFilms	780 nm and 1550 nm coatings on windows

A.2 Lasers, Fibers, AOMs, EOMs, Optoisolators

Part Number **Vendor**	**Part Description**
DLX-110 Toptica Photonics Inc.	780 nm, 750 mW tapered amplifier diode laser
—- Toptica Photonics Inc.	laser controller
ELR-15K-LP-SF IPG Photonics	1550 nm, 15 W fiber laser
TEC A00-Littrow TEC series Sacherlaser	780 nm, 100 mW diode laser
—- Sacherlaser	laser controller
TIS-SF-07 ring laser Tekhnoscan	800 nm tunable Ti-Sapphire Laser
Verdi-10W	532 nm , 10 W Verdi, controller, cooler

Coherent	
—- Canadian Instrumentation	custom 4× 4 fiber splitter
2007 New Focus	Nirvana detector
1206C-2-840B Isomet	80 MHz AOM, coating-780
DE-802MN IntraAction	Deflection driver, 80 MHz
360-40, 302RM ConOptics	EOM, EOM driver, for dipole trap
4002-Visible New Focus	EOM, laser lock

A.3 Power Supplies

Part Number **Vendor**	**Part Description**
DLM-600 Elgar Electronics	Sorensen 8V-75A power supply
XLT-60 Elgar Electronics	Sorensen 4V-15A power supply
ATE 15-3 Test Equity	Kepco 1/4 rack supply
ATE 3-10 Test Equity	Kepco 1/2 rack supply
HP 6269B Ebay	HP linear supply DC 0-40 V, 0-50 A

A.4 Miscellaneous parts and notable electronic bits

Part Number	**Part Description**

Vendor	
LS6T2 Uniblitz	mechanical shutter
TIA 1000-1-R8 MiniCircuits	35 dB gain RF power amplifier
PTS 160 Ebay	Frequency synthesizer
ABL-200-40-10-LT40AS-NC Aerotech	air-bearing stage
LB1005 Precision Photonics	Lock box
09F2013, 09F2384, 09F2213 Newark	Varistor, littlefuse
96B6121 originally international rectifier, but has been sold; check Newark	IGBT (GA200SA60U)
MJ4502G Newark	Darlington high current MOSFET, OnSemi

Bibliography

[1] M.H. Anderson, J.R. Ensher, M.R. Matthews, C.E. Wieman, and E.A. Cornell. Observation of Bose-Einstein condensation in a dilute atomic vapor. *Science*, 269:198, 1995.

[2] Neil W. Ashcroft and N. David Mermin. *Solid State Physics*. Brooks Cole, 1st edition, January 1976.

[3] S. Aubry and G. André. Analyticity breaking and Anderson localization in incommensurate lattices. *Ann. Israel. Phys. Soc.*, 3:133, 1980.

[4] Weizhu Bao, Dieter Jaksch, and Peter A. Markowich. Numerical solution of the Gross-Pitaevskii equation for Bose-Einstein condensate. *Journal of Computational Physics*, 187:318, 2003.

[5] Thomas E. Barrett, Samuel W. Dapore-Schwartz, Mark D. Ray, and Gregory P. Lafyatis. Slowing atoms with σ^- polarized light. *Phys. Rev. Lett.*, 67(25):3483, 1991.

[6] Juliette Billy, Vincent Josse, Zhanchun Zuo, Alain Bernard, Ben Hambrecht, Pierre Lugan, David Clément, Laurent Sanchez-Palencia, Phillipe Bouyer, and Alain Aspect. Direct oberservation of Anderson localization of matter waves in a controlled disorder. *Nature*, 453:891, 2008.

[7] Eric D. Black. An introduction to Pound-Drever-Hall laser frequency stabilization. *Am. J. Phys*, 69(1):79, 2001.

[8] Immanuel Bloch, Jean Dalibard, and Wilhelm Zwerger. Many-body physics and ultracold gases. *Rev. Mod. Phys.*, 80:885, 2008.

[9] Steven Chu, L. Hollberg, J.E. Bjorkholm, Alex Cable, and A. Ashkin. Three-dimensional viscous confinement and cooling of atoms by resonance radiation pressure. *Phys. Rev. Lett.*, 55:48, 1985.

[10] Kristan L. Corwin, Zheng-Tian Lu, Carter F. Hand, Ryan J. Epstein, and Carl E. Wieman. Frequency-stabilized diode laser with the Zeeman shift in an atomic vapor. *Applied Optics*, 37(15):3295, 1998.

[11] M. Cristiani, O. Morsch, J.H. Müller, D. Ciampini, and E. Arimondo. Experimental properties of Bose-Einstein condensates in one-dimensional optical lattices: Bloch oscillations, Landau-Zener tunneling and mean-field effects. *Phys. Rev. A*, 65:063612, 2002.

[12] Franco Dalfovo, Stefano Giorgini, Lev. P. Pitaevskii, and Sandro Stringari. Theory of Bose-Einstein condesation of dilute gases. *Rev. Mod. Phys.*, 71:463–512, 1999.

[13] B. Damski, J. Zakrzewski, L. Santos, P. Zoller, and M. Lewenstein. Atomic Bose and Anderson glasses in optical lattices. *Phys. Rev. Lett.*, 91(8):080403, 2003.

[14] K.B. Davis, M.-O. Mewes, M.R. Andrews, N.J. Van Druten, D.S. Durfee, D.M. Kurn, and W. Ketterle. Bose-Einstein condensation in a gas of sodium atoms. *Phys. Rev. Lett.*, 75:3969, 1995.

[15] Wolfgang Demtroeder. *Laser Spectroscopy: Basic concepts and instrumentation*. Springer, 3rd edition, November 2002.

[16] J. Hecker Denschlag, J. E. Simsarian, H. Haffner, C. McKenzie, A. Browaeys, D. Cho, K. Helmerson, S.L. Rolston, and W.D. Phillips. Bose-Einstein condensate in an optical lattice. *J. Phys. B.*, 35:3095, 2002.

[17] Roberto B. Diener, Georgios A. Georgakis, Jianxin Zhong, Mark Raizen, and Qian Niu. Transition between extended and localized states in a one-dimensional incommensurate optical lattice. *Phys. Rev. A*, 64:033416, 2001.

[18] Elizabeth A. Donley, Neil R. Claussen, Simon L. Cornish, Jacob L. Roberts, Eric A. Cornell, and Carl E. Wieman. Dynamics of collapsing and exploding Bose-Einstein condensates. *Nature*, 412(19):295, 2001.

[19] G.J. Duffy, A.S. Mellish, K.J. Challis, and A.C. Wilson. Nonlinear atom-optical δ-kicked harmonic oscillator using a Bose-Einstein condensate. *Phys. Rev. A*, 70:041602(R), 2004.

[20] J. Dziarmaga, A. Smerzi, W.H. Zurek, and A.R. Bishop. Dynamics of quantum phase transition in an array of Josephson junctions. *Phys. Rev. Lett.*, 88:167001, 2002.

[21] E. Edwards, M. Beeler, Tao Hong, and S.L. Rolston. Adiabaticity and localization in incommensurate lattices. *Phys. Rev. Lett.*, 101:260402, 2008.

[22] M.P.A. Fisher, P.B. Weichman, G. Grinstein, and D.S. Fisher. Boson localization and the superfluid-insulator transition. *Phys. Rev. B*, 40:546, 1989.

[23] A. Flesch, M. Cramer, I.P. McCulloch, U. Schollwöck, and J. Eisert. Probing local relaxation of cold atoms in optical superlattices. *Phys. Rev. A*, 78:033608, 2008.

[24] J. Fortagh, A. Grossmann, T.W. Hänsch, and C. Zimmermann. Fast loading of a magneto-optical trap from a pulsed thermal source. *J. App. Phys.*, 84(12):6499, 1998.

[25] S.A. Gardiner, D. Jaksch, R. Dum, J.I. Cirac, and P. Zoller. Nonlinear matter wave dynamics with a chaotic potential. *Phys. Rev. A*, 62:023612, 2000.

[26] Markus Greiner et al. Quantum phase transition from a superfluid to a Mott insulator in a gas of ultracold atoms. *Nature*, 415:39, 2002.

[27] D.R. Grempel, Shmuel Fishman, and R.E. Prange. Localization in an incommensurate potential: An exactly solvable model. *Phys. Rev. Lett.*, 49(11):833, 1982.

[28] Rudolf Grimm, Matthias Weidemuller, and Yurii B. Ovchinnikov. Optical dipole traps for neutral atoms. *Adv. At. Mol. Opt. Phys.*, 42:95, 2000.

[29] L. Guidoni, C. Triche, P. Verkerk, and G. Grynberg. Quasiperiodic optical lattices. *Phys. Rev. Lett.*, 79(18):3363, 1997.

[30] J. Dziarmaga H. Arodz and W.H. Zurek, editors. *Patterns of symmetry breaking*, Cracow, Poland, September 2003. Proceedings of the NATO Advanced Study Institute on Patterns of Symmetry Breaking, Kluwer Academic Publishers.

[31] M. Holthaus, G.H. Ristow, and D.W. Hone. Random lattices in combined a.c. and d.c. electric fields: Anderson vs. Wannier-Stark localization. *Europhys. Lett.*, 32:241, 1995.

[32] V.V. Ivanov, A. Alberti, M. Schioppo, G. Ferrari, M. Artoni, M.L. Chiofalo, and G.M. Tino. Coherent delocalization of atomic wave packets in driven lattice potentials. *Phys. Rev. Lett*, 100:043602, 2008.

[33] B.D. Josephson. Coupled superconductors. *Rev. Mod. Phys.*, 36:216, 1964.

[34] P.S. Julienne, C.J. Williams, Y.B. Band, and Marek Trippenbach. Loading Bose-Einstein condensed atoms into the ground state of an optical lattice. *Phys. Rev. A*, 72:053615, 2005.

[35] G.A. Kells, J. Twamley, and D.M. Hefferman. Dynamical properties of the delta-kicked harmonic oscillator. *Phys. Rev. E*, 70:015203, 2004.

[36] Wolfgang Ketterle and N.J. Van Druten. Evaporative cooling of trapped atoms. *Adv. At. Mol. Opt. Phys.*, 37:181, 1996.

[37] T.W.B. Kibble. Topology of cosmic domains and strings. *J. Phys. A*, 9:1387, 1976.

[38] D. Kleppner, T.J. Greytak, T.C. Killian, D.G. Fried, L. Willmann, D. Landhuis, and S.C. Moss. *Bose-Einstein Condensation in Atomic Gases, Proceedings of the international school of Physics "Enrico Fermi," Course CXL.* IOS Press, Amsterdam, 1999.

[39] P.J. Lee, M. Anderlini, B.L. Brown, J. Sebby-Strabley, W.D. Phillips, and J.V. Porto. Sublattice addressing and spin-dependent motion of atoms in a double well lattice. *Phys. Rev. Lett.*, 99:020402, 2007.

[40] J.E. Lye, L. Fallani, C. Fort, V. Guarrera, Michele Modugno, D.S. Wiersma, and Massimo Inguscio. Effect of interactions on the localization of a Bose-Einstein condensate in a quasiperiodic lattice. *Phys. Rev. A*, 75:061603, 2007.

[41] J.E. Lye, L. Fallani, Michele Modugno, D.S. Wiersma, C. Fort, and Massimo Inguscio. Bose-Einstein condensate in a random potential. *Phys. Rev. Lett.*, 95:070401, 2005.

[42] Harold J. Metcalf and Peter van der Straten. *Laser Cooling and Trapping*. Graduate Texts in Contemporary Physics. Springer, New York, 1999.

[43] Michele Modugno. Collective dynamics and expansion of a Bose-Einstein condensate in a random potential. *Phys. Rev. A*, 73:013606, 2006.

[44] F.L. Moore, J.C. Robinson, C. Bharucha, P.E. Williams, and M.G. Raizen. Observation of dynamical localization in atomic momentum transfer: A new testing ground for quantum chaos. *Phys. Rev. Lett.*, 73:2974, 1994.

[45] Oliver Morsch and Markus Oberthaler. Dynamics of Bose-Einstein condensates in optical lattices. *Rev. Mod. Phys.*, 78:179, 2006.

[46] Yu. B. Ovchinnikov, J.H. Müller, M.R. Doery, E.J.D. Vrendenbregt, K. Helmerson, S.L. Rolston, and W.D. Phillips. Diffraction of a released Bose-Einstein condensate by a pulsed standing light wave. *Phys. Rev. Lett.*, 83(2):284, 1999.

[47] S. Peil, J.V. Porto, B. Laburthe Tolra, J.M. Obrecht, M. Subbotin, S. L. Rolston, and W.D. Phillips. Patterned loading of a Bose-Einstein condensate into an optical lattice. *Phys. Rev. A*, 67:051603, 2003.

[48] C.J. Pethick and H. Smith. *Bose-Einstein Condensation in Dilute Gases*. Cambridge University Press, New York, 2002.

[49] Anatoli Polkovnikov and Vladimir Gritsev. Breakdown of the adiabatic limit in low-dimensional gapless systems. *Nature Physics*, 4:478, May 2008.

[50] E. Raab, M. Prentiss, A. Cable, S. Chu, and D. Pritchard. Trapping of neutral-sodium atoms with radiation pressure. *Phys. Rev. Lett.*, 59:2631, 1987.

[51] Umakant D. Rapol, Ajay Wasan, and Vasant Natarajan. Loading of a Rb magneto-optic trap from a getter source. *Phys. Rev. A*, 64:023402, 2001.

[52] J. Reichel, W. Hänsel, and T.W. Hänsch. Atomic micromanipulation with magnetic surface traps. *Phys. Rev. Lett.*, 83:3398, 1999.

[53] Giacomo Roati, Chiara D'Errico, Leonardo Fallani, Marco Fattori, Chiara Fort, Matteo Zaccanti, Giovanni Modugno, Michele Modugno, and Massimo Inguscio. Anderson localization of a non-interacting Bose-Einstein condensate. *Nature*, 453:895, 2008.

[54] R. Roth and K. Burnett. Phase diagram of bosonic atoms in two-color superlattices. *Phys. Rev. A.*, 68:023604, 2003.

[55] G. Roux, T. Barthel, I.P. McCulloch, C. Kollath, U. Schollwöck, and T. Giamarchi. Quasiperiodic Bose-Hubbard model and localization in one-dimensional cold atomic gases. *Phys. Rev. A*, 78:023628, 2008.

[56] L. Sanchez-Palencia, D. Clément, P. Lugan, P. Bouyer, G.V. Shlyapnikov, and A. Aspect. Anderson localization of expanding Bose-Einstein condensates in random potentials. *Phys. Rev. Lett.*, 98:210407, 2007.

[57] L. Sanchez-Palencia and L. Santos. Bose-Einstein condensate in optical quasicrystal lattices. *Phys. Rev. A*, 72:053607, 2005.

[58] L. De Sarlo, L. Fallani, J.E. Lye, M. Modugno, C. Fort, and M. Inguscio. Unstable regimes for a Bose-Einstein condensate in an optical lattice. *Phys. Rev. A*, 72:013603, 2005.

[59] L.I. Schiff. *Quantum Mechanics*. McGraw-Hill, New York, 1955.

[60] T. Schulte, S. Drenkelforth, G. Kleine Büning, W. Ertmer, J. Arlt, M. Lewenstein, and L. Santos. Dynamics of Bloch oscillations in disordered lattice potentials. *Phys. Rev. A*, 77:023610, 2008.

[61] T. Schulte, S. Drenkelforth, J. Kruse, W. Ertmer, J . Arlt, K. Sacha, J. Zakrzewski, and M. Lewenstein. Route towards Anderson-like localization of Bose-Einstein condensates in disorder optical lattices. *Phys. Rev. Lett.*, 95:170411, 2005.

[62] Daniel A. Steck. Rubidium 87 line data. available online at http://steck.us/alkalidata, (revision 2.0.1, 2 May 2008).

[63] M.R. Walkiewicz, P.J. Fox, and R.E. Scholten. Candlestick rubidium beam source. *Rev. Sci. Instrum.*, 71:3342, 2000.

[64] C.N. Weiler, T.W. Neely, D.R. Scherer, A.S. Bradley, M.J. Davis, and B.P. Anderson. Spontaneous vortices in the formation of Bose-Einstein condensates. *Nature*, 455:948, 2008.

[65] David S. Weiss, Erling Riis, Yaakov Shevy, P. Jeffrey Ungar, and Steven Chu. Optical molasses and multilevel atoms: experiment. *J. Opt. Soc. Am. B*, 6(11):2072, November 1989.

[66] M. White, M. Pasienski, D. McKay, S. Zhou, D. Ceperley, and B. Demarco. Strongly interacting bosons in a disordered optical lattice. *e-print cond-mat/0807.0446*, 2008.

[67] S. Wildermuth, P. Krüger, C. Becker, M. Brajdic, S. Haupt, A. Kasper, R. Folman, and J. Schmiedmayer. Optimized magneto-optical trap for experiments with ultracold atoms near surfaces. *Phys. Rev. A*, 69:030901, 2004.

[68] W.H. Zurek. Cosmological experiments in superfluid helium? *Nature (London)*, 317:505, 1985.